Turbulent cascade in fully developed turbulent channel flow

A. Apostolidis[1], J.P. Laval[1] and J.C. Vassilicos[1],†

[1]Univ. Lille, CNRS, ONERA, Arts et Metiers Institute of Technology, Centrale Lille, UMR 9014 – LMFL – Laboratoire de Mécanique des Fluides de Lille – Kampé de Fériet, F-59000 Lille, France

We show that Kolmogorov scale-by-scale equilibrium in the intermediate layer of a fully developed turbulent channel flow is only achieved asymptotically around the Taylor length and, therefore, not in an inertial range. Furthermore, we analyse scale-by-scale turbulence production and interscale turbulence energy transfer in terms of alignments/anti-alignments of fluctuating velocities, straining/compressive relative motions, forward/inverse interscale transfer/cascade and homogeneous/non-homogeneous interscale transfer rate contributions. We also propose leading order scalings for second- and third-order two-point statistics, including the extremum interscale turbulence energy transfer rate and a second-order anisotropic structure function, which acts as a scale-by-scale Reynolds shear stress and determines the scale-by-scale (two-point) turbulence production rate.

Key words: turbulence theory, channel flow

1. Introduction

The Kolmogorov theory of equilibrium cascade works best for statistically stationary and homogeneous turbulence where the power input balances the dissipation rate and predicts that the interscale transfer rate balances the turbulence dissipation rate in an inertial range of scales (Batchelor 1953; Frisch 1995; Lesieur 1997). In particular, this inertial range equilibrium cascade leads to the well-known turbulence dissipation scaling (Batchelor 1953; Sreenivasan 1984; Vassilicos 2015) first introduced by Taylor (1935) without justification. In statistically homogeneous but non-stationary, in particular decaying, turbulence, the situation is different. Specifically, there is a non-equilibrium turbulence dissipation scaling initially during decay (Vassilicos 2015; Goto & Vassilicos 2016),

† Email address for correspondence: john-christos.vassilicos@centralelille.fr

followed at later times by the classical turbulence dissipation as a result of balanced non-equilibrium (Goto & Vassilicos 2016; Steiros 2022) rather than Kolmogorov equilibrium throughout an inertial range.

Lundgren (2002) applied a matched asymptotic expansion approach to freely decaying homogeneous isotropic turbulence far from initial conditions, which led to the conclusion that the interscale transfer rate has an extremum at a length scale r_{max} that is proportional to the Taylor length λ. Wind tunnel data of nominally freely decaying homogeneous isotropic turbulence (Obligado & Vassilicos 2019) confirm $r_{max} \approx 1.5\lambda$ and EDQNM simulations of such turbulence (Meldi & Vassilicos 2021) confirm $r_{max} \approx 1.12\lambda$ for $Re_\lambda = 10^2$ to 10^6. Hence, Kolmogorov equilibrium in non-stationary, in fact freely decaying far from initial conditions, statistically homogeneous isotropic turbulence seems to be achieved asymptotically only around λ; and not in an inertial range given that λ depends on viscosity and total turbulent kinetic energy, and that there is a systematic departure from equilibrium (most clearly demonstrated in Meldi & Vassilicos 2021) when moving away from λ, both towards the integral scale and towards the Kolmogorov length η.

Diverting attention from homogeneous non-stationary turbulence to stationary non-homogeneous turbulence, we ask about the validity of Kolmogorov equilibrium in stationary non-homogeneous conditions and chose to focus in this paper on fully developed turbulent channel flow (FD TCF). This is a statistically stationary non-homogeneous turbulent flow where turbulence production approximately balances turbulence dissipation (similarly to statistically stationary homogeneous turbulence) in some very significant region of space, the intermediate layer where the log-law of the wall has been traditionally claimed. Is there an average equilibrium between interscale turbulence energy transfer rate and turbulence dissipation in the intermediate layer of FD TCF where turbulence production approximately balances turbulence dissipation? If so, in what range of length scales, inertial or not? What processes are involved in the scale-by-scale turbulence energy balance in that range, if there is one, and outside it? What is the role of inhomogeneity, in particular in terms of scale-by-scale turbulence production but also directly on interscale energy transfer? What type of flow motions underpin interscale turbulence energy transfers and scale-by-scale turbulence production (referred to as two-point turbulence production in the remainder of this paper)?

In the following section, we introduce the scale-by-scale turbulence energy balance in its most general form and the spherical average operation, which we use to simplify it for this study. Section 3 is a brief description of the FD TCF DNS data we use for our post-processing. In §4, we simplify the spherically averaged scale-by-scale turbulence energy balance for the particular case of the intermediate layer of an FD TCF and in §5, we examine the two-point turbulence production term which appears in this balance. Section 6 deals with second- and third-order structure functions and interscale turbulence energy transfer by adapting to FD TCF the matched asymptotic expansion approach of Lundgren (2002), and then we compare the results to the DNS data in §7. Finally, §8 introduces two decompositions of the interscale turbulence energy transfer rate and attempts to answer the questions of non-homogeneity's role and of what flow motions are responsible for which aspects of interscale turbulence energy transfer. In §9, we summarise our conclusions.

2. Scale-by-scale turbulence energy balance

To analyse the turbulent energy cascade in turbulent channel flow, we use a Kármán–Howarth–Monin–Hill (KHMH) equation which is a scale-by-scale energy budget equation in its most general form without any assumptions about the flow (Hill 2001, 2002). The form of the KHMH equation that we use is an evolution equation for $|\delta \boldsymbol{u}|^2$,

where $\delta u \equiv u(x + r/2, t) - u(x - r/2, t)$ is the difference between fluctuating velocities at two points $\xi^+ \equiv x + r/2$ and $\xi^- \equiv x - r/2$ in the flow where the separation vector $r = (r_1, r_2, r_3)$ gives some sense of scales. The centroid $x = (x_1, x_2, x_3)$ is mid-way between these two points.

A Reynolds decomposition $U + u$ is used for the velocity field in this form of the KHMH equation where $U = (U_1, U_2, U_3)$ is the mean flow. The KHMH equation follows directly from the incompressible Navier–Stokes equations and, with notation $U_i^\pm \equiv U_i(x \pm r/2)$, $u_i^\pm \equiv u_i(x \pm r/2)$ and $\delta p \equiv p(x + r/2, t) - p(x - r/2, t)$, where p is the fluctuating pressure field (normalised by the constant density), reads as follows:

$$
\underbrace{\frac{\partial \langle |\delta u|^2 \rangle}{\partial t}}_{A_t} + \underbrace{\frac{U_i^+ + U_i^-}{2} \frac{\partial \langle |\delta u|^2 \rangle}{\partial x_i}}_{A} + \underbrace{\frac{\partial \langle \delta u_i |\delta u|^2 \rangle}{\partial r_i}}_{\Pi} + \underbrace{\frac{\partial \delta U_i \langle |\delta u|^2 \rangle}{\partial r_i}}_{\Pi_U}
$$

$$
= \underbrace{-2 \langle \delta u_i \delta u_j \rangle \frac{\partial \delta U_j}{\partial r_i} - \langle (u_i^+ + u_i^-) \delta u_j \rangle \frac{\partial \delta U_j}{\partial x_i}}_{\mathcal{P}} - \underbrace{\frac{\partial \left\langle \frac{u_i^+ + u_i^-}{2} |\delta u|^2 \right\rangle}{\partial x_i}}_{T_u} - \underbrace{2 \frac{\partial \langle \delta u_i \delta p \rangle}{\partial x_i}}_{T_p}
$$

$$
+ \underbrace{\nu \frac{1}{2} \frac{\partial^2 \langle |\delta u|^2 \rangle}{\partial x_i^2}}_{D_x} + \underbrace{2\nu \frac{\partial^2 \langle |\delta u|^2 \rangle}{\partial r_i^2}}_{D_r} - \underbrace{\left[2\nu \left\langle \left(\partial u_j^- / \partial \xi_i^- \right)^2 \right\rangle + 2\nu \left\langle \left(\partial u_j^+ / \partial \xi_i^+ \right)^2 \right\rangle \right]}_{\varepsilon},
$$

$$
\tag{2.1}
$$

where the brackets $\langle \cdot \rangle$ denote the averaging operation on which the Reynolds decomposition is based. The KHMH equation includes the following terms:

(i) $A_t = \partial \langle |\delta u|^2 \rangle / \partial t$ is the time derivative term;
(ii) $A = (U_i^+ + U_i^-)/2)(\partial \langle |\delta u|^2 \rangle / \partial x_i)$ is the mean advection term;
(iii) $\Pi = \partial \langle \delta u_i |\delta u|^2 \rangle / \partial r_i$ is the nonlinear interscale transfer rate of $|\delta u|^2$ by turbulent fluctuations in scale space and thus directly linked to the energy cascade;
(iv) $\Pi_U = \partial \delta U_i \langle |\delta u|^2 \rangle / \partial r_i$ is the linear interscale transfer rate of $|\delta u|^2$ in scale space by mean velocity differences;
(v) $\mathcal{P} = -2 \langle \delta u_i \delta u_j \rangle (\partial \delta U_j / \partial r_i) - \langle (u_i^+ + u_i^-) \delta u_j \rangle (\partial \delta U_j / \partial x_i)$ is the two-point production of $|\delta u|^2$ by the mean shear;
(vi) $T_u = \partial \langle ((u_i^+ + u_i^-)/2) |\delta u|^2 \rangle / \partial x_i$ is the turbulent transport of $|\delta u|^2$ in physical space;
(vii) $T_p = 2(\partial \langle \delta u_i \delta p \rangle / \partial x_i)$ is the pressure-velocity term;
(viii) $D_x = (\nu/2)(\partial^2 \langle |\delta u|^2 \rangle / \partial x_i^2)$ is the viscous diffusion in physical space;
(ix) $D_r = 2\nu (\partial^2 \langle |\delta u|^2 \rangle / \partial r_i^2)$ is the viscous diffusion in scale space;
(x) $\varepsilon = 2\nu \langle (\partial u_j^- / \partial \xi_i^-)^2 \rangle + 2\nu \langle (\partial u_j^+ / \partial \xi_i^+)^2 \rangle$ is the two-point averaged turbulence pseudo-dissipation rate which is very close to the actual turbulence dissipation rate (e.g. see Pope 2000).

At this stage, we specialise this equation to FD TCF by choosing the averaging operation $\langle \cdot \rangle$ to be over the streamwise and spanwise homogeneous directions, i.e. over coordinates $x \equiv x_1$ (streamwise) and $z \equiv x_3$ (spanwise), and over time. The wall-normal coordinate is $y \equiv x_2$. Note that $U_2 = U_3 = 0$ and that this averaging operation implies $A_t = 0 = A$.

In non-homogeneous and non-isotropic turbulent flows (such as FD TCF), energy transfers and exchanges, including the turbulence cascade, are anisotropic. This equation has been studied extensively in FD TCF by Marati, Casciola & Piva (2004), Cimarelli & De Angelis (2012), Cimarelli, De Angelis & Casciola (2013), Cimarelli *et al.* (2016) and Gatti *et al.* (2019). In this paper, we concentrate our interest on the directionally averaged energy transfers by applying to each term of the KHMH equation an additional average over spheres in *r*-space. We therefore work with

$$\Pi^v + \Pi^v_U = \mathcal{P}^v + T^v_u + T^v_p + D^v_x + D^v_r - \varepsilon^v, \tag{2.2}$$

where (following Zhou & Vassilicos (2020) and §2 of Chen & Vassilicos (2022)) every term is obtained from its analogue in (2.1) by the application of the normalised three-dimensional (3-D) integral $(3/4\pi r^3) \int_{S(r)} \mathrm{d}^3 r$, $S(r)$ being the sphere of radius r in *r*-space; for example, $\Pi^v \equiv (3/4\pi r^3) \int_{S(r)} \Pi \, \mathrm{d}^3 r$, $\Pi^v_U \equiv (3/4\pi r^3) \int_{S(r)} \Pi_U \, \mathrm{d}^3 r$, $\mathcal{P}^v \equiv (3/4\pi r^3) \int_{S(r)} \mathcal{P} \, \mathrm{d}^3 r$, etc.

This approach averages over and therefore ignores length-scale anisotropies and replaces *r* by its modulus $r = |r|$ as a single measure of length-scale. However, the fundamental anisotropy responsible for correlations between streamwise and wall-normal directions remains in the turbulence production term. Every term in (2.2) is a function of only *y* (spatial non-homogeneity variable) and *r* (length-scale variable).

In §3, we describe the data from direct numerical simulations (DNS) of FD TCF that we use in this paper. We describe these DNS data before starting our analysis of (2.2) to be able to test against these data certain aspects of our analysis as it proceeds.

3. DNS data

For our analysis, we use the DNS data of Lozano-Durán & Jiménez (2014) for FD TCF at $Re_\tau = 932$ and 2003, ($Re_\tau \equiv u_\tau \delta/\nu$, where ν is the kinematic viscosity, δ is the channel half-width, and u_τ is the skin friction velocity obtained by averaging over time and over streamwise coordinate *x* and spanwise coordinate *z* at the channel's solid wall $y = 0$). The domain size for both simulations is $L_x = 2\pi\delta$ in the streamwise and $L_z = \pi\delta$ in the spanwise directions. The Navier–Stokes equations have been solved by integrating the evolution equations in terms of the wall-normal vorticity and the Laplacian of the wall-normal velocity for an incompressible fluid. The Fourier spectral method was used for the spatial discretisation in the wall-parallel directions. For the discretisation in the wall-normal direction, Chebyshev polynomials were used in the $Re_\tau = 932$ case, whereas a seven-point compact finite difference scheme was used in the $Re_\tau = 2003$ case. Finally, a third-order semi-implicit Runge–Kutta method with CFL = 0.5 was chosen for time advancement. A comparison of the two datasets can be found in Table 1 (the superscript [+] refers to non-dimensionalisation with wall units $\delta_\nu \equiv \nu/u_\tau$ for length and δ_ν/u_τ for time). We focus our DNS data analysis on the wall-normal locations that correspond to the region where the average production rate of turbulent kinetic energy roughly balances the average turbulence dissipation rate as identified by Apostolidis, Laval & Vassilicos (2022), i.e. $60 \leq y^+ \leq Re_\tau/2$.

Name	Re_τ	L_x/δ	L_z/δ	Δx^+	Δz^+	N_y	dt^+	N_t
LJ950	932	2π	π	11.5	5.7	385	8	3151
LJ2000	2003	2π	π	12.3	6.2	633	25	462

Table 1. DNS databases.

4. Scale-by-scale turbulent energy balance in the one-point average equilibrium range of FD TCF

We now examine (2.2) in the region of FD TCF, where the average one-point turbulence production rate is in approximate equilibrium with the average turbulence dissipation rate at a given y. This is a region of distances y from the bottom wall (where $y = 0$) such that $\delta_v \ll y \ll \delta$ (in the limit $Re_\tau = \delta/\delta_v \gg 1$) and where, classically, the mean flow velocity $U = (U_1, 0, 0)$ is expected to be logarithmic (e.g. see Pope 2000). Whilst previous works have suggested some not insignificant deviations from a log dependence on y of U_1 (e.g. see Vassilicos *et al.* 2015), in this work, we assume that the log law accounts for most of U_1, which implies that $\Pi_U = (\partial/\partial r_1)(\delta U_1\langle|\delta u|^2\rangle)$ is close to 0 in the region $\delta_v \ll y \ll \delta$ if $r_2 \ll 2y$ because $\delta U_1 = (u_\tau/\kappa)\ln(1 + r_2/y)/(1 - r_2/y) \approx 0$ (κ is the von Kármán dimensionless coefficient and note that wall blocking implies that r_2 is necessarily smaller or equal to $2y$). The DNS data confirm the prediction that Π_U^v is close to zero, see figure 1(*c,d*). We also make the assumption that turbulence is well mixed in this region and therefore assume that the physical-space divergence term $T_u^v + T_p^v$ is negligible. Whilst the DNS data support this assumption, see figure 1(*a,b*), it must be stressed that pressure plays an important redistributive role and that spatial energy transfer is not fully absent in the intermediate layer (e.g. Lozano-Durán & Jiménez 2014; Cimarelli *et al.* 2016; Lee & Moser 2019). The numerical details behind our calculations of normalised 3-D integrals $(3/4\pi r^3)\int_{S(r)} d^3r$, and in particular of terms such as $T_u^v = (3/4\pi r^3)\int_{S(r)} T_u d^3r$ and $T_p^v = (3/4\pi r^3)\int_{S(r)} T_p d^3r$, are given in the Appendix.

We therefore neglect both Π_U^v and $T_u^v + T_p^v$ from (2.2) and are left with

$$\Pi^v \approx \mathcal{P}^v + D_x^v + D_r^v - \varepsilon^v \qquad (4.1)$$

for $r_2 \ll 2y$ in the intermediate layer $\delta_v \ll y \ll \delta$.

By application of the Gauss divergence theorem, the interscale transfer rate takes the form

$$\Pi^v = \frac{3}{4\pi}\int\left\langle\frac{\delta u \cdot \hat{r}}{r}|\delta u|^2\right\rangle d\Omega_r \equiv \frac{S_3(r,y)}{r}, \qquad (4.2)$$

where Ω_r is the solid angle in r space and $\hat{r} \equiv r/|r|$. By distinguishing between radial and solid angle integrations in r-space, the viscous diffusion terms become

$$D_x^v + D_r^v = \frac{3\nu}{8\pi r^3}\int_0^r \rho^2 \frac{d^2 S_2}{dy^2}(\rho, y)\, d\rho + \frac{3\nu}{\pi r}\frac{dS_2}{dr}(r, y), \qquad (4.3)$$

where

$$S_2(r, y) \equiv \int\langle|\delta u|^2\rangle d\Omega_r. \qquad (4.4)$$

In FD TCF, the production term $\mathcal{P}^v$ is obtained by applying the integral operation $(3/4\pi r^3)\int_{S(r)} d^3r$ on $-2\langle\delta u_2\delta u_1\rangle(\partial\delta U_1/\partial r_2) - \langle(u_2^+ + u_1^-)\delta u_1\rangle(\partial\delta U_1/\partial y)$.
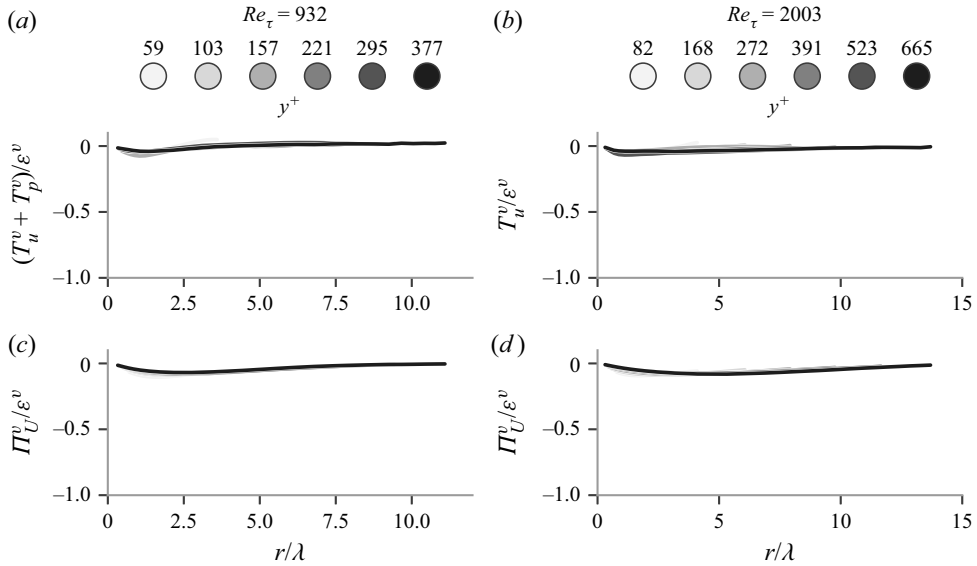
Figure 1. (a) Turbulent transport T_u plus pressure-velocity term T_p, integrated over the volume of sphere with radius r, normalised by the volume integral of the two point dissipation rate ε as a function of r/λ for $Re_\tau = 932$, (b) T_u^v/ε^v for $Re_\tau = 2003$ (T_p is unavailable from the recorded DNS data at $Re_\tau = 2003$), (c) volume integral of linear interscale transfer term divided with ε^v Π_U^v/ε^v for $Re_\tau = 932$ and (d) for $Re_\tau = 2003$. Wall-normal distance is increased from light to dark colours ($y^+ = 59$ to 377 for $Re_\tau = 932$, $y^+ = 82$ to 665 for $Re_\tau = 2003$). The normalisation by the Taylor length λ (defined in § 6.3) is arbitrary in these plots.

Targeting again the intermediate region $\delta_\nu \ll y \ll \delta$, where the log law $\mathrm{d}U_1/\mathrm{d}y \approx u_\tau/\kappa y$ might be considered to be a good approximation in the limit $\delta/\delta_\nu \gg 1$ (κ is the von Kármán dimensionless coefficient), the two-point production term becomes

$$\mathcal{P}^v \approx -\frac{u_\tau^3}{\kappa y}\frac{3}{4\pi r^3}\int_0^r \rho^2 \left[\frac{S_{12}(\rho, y)}{u_\tau^2} - \frac{S_{1\times 2}(\rho, y)}{u_\tau^2}\right]\mathrm{d}\rho \tag{4.5}$$

in this intermediate region, where

$$S_{12}(r, y) \equiv 2\int \langle \delta u_2 \delta u_1 \rangle \left[1 - \left(\frac{r_2}{2y}\right)^2\right]^{-1}\mathrm{d}\Omega_r \tag{4.6}$$

and

$$S_{1\times 2}(r, y) \equiv \int \langle (u_2^+ + u_2^-)\delta u_1 \rangle (r_2/y)\left[1 - \left(\frac{r_2}{2y}\right)^2\right]^{-1}\mathrm{d}\Omega_r. \tag{4.7}$$

We expect $S_{1\times 2}(r, y)$ to be much smaller in magnitude than $S_{12}(r, y)$, in fact even close to vanishing, because of the expected decorrelation between wall-normal velocity fluctuations effectively larger than r (i.e. $u_2^+ + u_2^-$) and streamwise velocity fluctuations effectively smaller than r (i.e. δu_1). This is confirmed by the DNS data in figure 2, which also show that $S_{12}(r, y)$ is negative for all $r \le 2y$ irrespective of y (because of wall blocking, r cannot be larger than $2y$, and because of the integrand's singularity in the definitions of $S_{1\times 2}(r, y)$ and $S_{12}(r, y)$, we plot them for $r \le 2y - 8\delta_\nu$ throughout
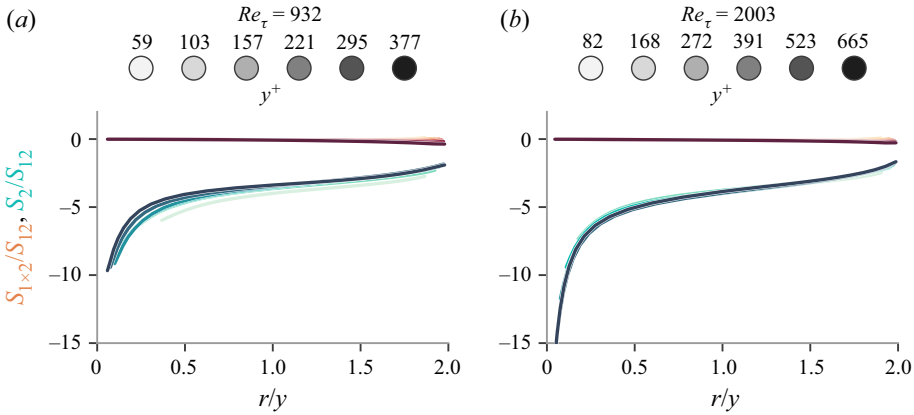
967 A22-6

Figure 2. Ratios of $S_{1\times2}$ in orange colours and S_2 in marine colours over S_{12} for different normalised scales r/y. Wall-normal distance is increased from light to dark colours as in figure 1. (a) $Re_\tau = 932$, (b) $Re_\tau = 2003$.

the paper). In the intermediate region, where the log law of the wall might be expected to hold, we therefore have a positive two-point production term given, to good approximation, by

$$\mathcal{P}^v \approx -\frac{u_\tau^3}{\kappa y}\frac{3}{4\pi r^3}\int_0^r \rho^2 \frac{S_{12}(\rho, y)}{u_\tau^2}\,\mathrm{d}\rho. \tag{4.8}$$

Bringing together (4.2), (4.3) and (4.8) into (4.1), we obtain the following two-point energy balance valid for $r_2 \ll 2y$ and $\delta/\delta_v \gg 1$ in the intermediate region $\delta_v \ll y \ll \delta$ of FD TCF:

$$\frac{S_3(r, y)}{r} - \frac{3v}{8\pi r^3}\int_0^r \rho^2 \frac{\mathrm{d}^2 S_2}{\mathrm{d}y^2}(\rho, y)\,\mathrm{d}\rho + \frac{3v}{\pi r}\frac{\mathrm{d}S_2}{\mathrm{d}r}(r, y)$$

$$\approx -\varepsilon^v - \frac{u_\tau^3}{\kappa y}\frac{3}{4\pi r^3}\int_0^r \rho^2 S_{12}(\rho, y)\,\mathrm{d}\rho. \tag{4.9}$$

In this equation, the first term on the left-hand side is the interscale transfer rate, the second and third terms on the left-hand side are the viscous diffusion terms, and the second term on the right-hand side is the two-point turbulence production rate. Before making use of this equation in §6, we look closer into the positive sign of the two-point turbulence production.

5. Two-point turbulence production

Here, $\mathcal{P}^v$ represents the rate with which turbulent kinetic energy is gained or lost by scales smaller than r if $\mathcal{P}^v$ is respectively positive or negative. Of course, we may expect energy to be gained in some r directions and lost in some other r directions: $\mathcal{P}^v$ represents the rate with which the aggregate energy averaged over all directions is gained or lost at scales smaller than r by the linear effects of mean flow gradients on the turbulence. This is not a nonlinear interscale mechanism relating to a turbulence cascade which is, in fact, represented by Π^v.

Turbulence production results from the interplay of non-isotropy in the form of non-zero Reynolds shear stresses with the mean flow gradient. In FD TCF, the one-point Reynolds shear stress is $\langle u_1 u_2 \rangle$ and it interacts with the mean flow gradient $\mathrm{d}U_1/\mathrm{d}x_2 = \mathrm{d}U_1/\mathrm{d}y$

to give the one-point turbulence production rate $-\langle u_1 u_2 \rangle (\mathrm{d}U_1/\mathrm{d}y)$ which is positive (i.e. creation of turbulent kinetic energy) because $\langle u_1 u_2 \rangle$ is negative. The negative sign of $\langle u_1 u_2 \rangle$ results from the predominance of turbulent transport towards the wall of forward streamwise fluctuating velocities and of turbulent transport away from the wall of backward streamwise fluctuating velocities. These turbulent momentum fluxes are partly caused by sweeps in the case of transport towards the wall and ejections in the case of transport away from the wall (Kline & Robinson 1990; Wallace 2016) and lead to the well-known increase by turbulence of wall shear stress and skin friction drag.

The two-point Reynolds shear stress $\langle \delta u_1 \delta u_2 \rangle$ results from anisotropies at scales comparable to r and smaller, and relates to the one-point shear stress by

$$\langle \delta u_1 \delta u_2 \rangle = (\langle u_1^+ u_2^+ \rangle - \langle u_1^+ u_2^- \rangle) + (\langle u_1^- u_2^- \rangle - \langle u_1^- u_2^+ \rangle). \tag{5.1}$$

One can expect the two-point Reynolds shear stress to have the same sign as the one-point shear stresses at $\boldsymbol{\xi}^+$ and $\boldsymbol{\xi}^-$ (which are known to be negative in FD TCF) if the magnitudes of the two-point correlations $\langle u_1^+ u_2^- \rangle$ and $\langle u_1^- u_2^+ \rangle$ are decreasing functions of distance between $\boldsymbol{\xi}^+$ and $\boldsymbol{\xi}^-$. The two-point Reynolds shear stress appears in the two-point turbulence production rate via S_{12} (see (4.8) and the definition in (4.6) of S_{12}) and we therefore define, for initial simplicity of interpretation, a two-point Reynolds shear stress integrated over the solid angle in r-space as follows: $\tilde{S}_{12}(r, y) \equiv \int \langle \delta u_2 \delta u_1 \rangle \, \mathrm{d}\Omega_r$. Defining additionally $\int \langle u_2^+ u_1^+ \rangle \, \mathrm{d}\Omega_r = \int \langle u_2^- u_1^- \rangle \, \mathrm{d}\Omega_r \equiv \tilde{R}_{12}(y, r)$ and $\int \langle u_2^+ u_1^- \rangle \, \mathrm{d}\Omega_r = \int \langle u_2^- u_1^+ \rangle \, \mathrm{d}\Omega_r \equiv \tilde{C}_{12}(r, y)$, (5.1) leads to

$$\tilde{S}_{12}(r, y) = 2\tilde{R}_{12}(y, r) - 2\tilde{C}_{12}(r, y) \tag{5.2}$$

in terms of solid angle-integrated one-point Reynolds shear stress $\tilde{R}_{12}(y, r)$ and solid angle-integrated two-point correlation $\tilde{C}_{12}(r, y)$. In figure 3(*a,b*), we use the DNS data to plot $\tilde{C}_{12}(r, y)/|\tilde{R}_{12}(y)|$ vs r (black lines) for the two Reynolds numbers available and for different values of wall distance y. In all cases, $\tilde{C}_{12}(r, y)/|\tilde{R}_{12}(y, r)|$ is a monotonically increasing function of r, from $\tilde{C}_{12}(r, y)/|\tilde{R}_{12}(y, r)| = -1$ at $r = 0$ towards 0 with increasing r. It follows from (5.2) that the solid angle-integrated two-point Reynolds stress inherits the negative sign of the solid angle-integrated one-point Reynolds shear stress but with reduced magnitude because of the negative two-point correlation $\tilde{C}_{12}(r, y)$, which is smaller in magnitude than $\tilde{R}_{12}(y, r)$ for all y and all $r \neq 0$.

Inheriting the sign of the one-point Reynolds shear stress means that for the two-point Reynolds shear stress, sweeps and ejections are contributing to its negative sign. However, the two-point correlation $\tilde{C}_{12}(r, y)$ reduces the proportion of this contribution. Assuming that fluctuating velocities may be approximately aligned within sweep and ejection events, particularly for the smaller values of r, we now use the DNS data to calculate correlations between u_2 and u_1 at two different points $\boldsymbol{\xi}^+$ and $\boldsymbol{\xi}^-$ conditionally on $\boldsymbol{u}^+ \cdot \boldsymbol{u}^- > 0$ for aligned pairs of fluctuating velocities and conditionally on $\boldsymbol{u}^+ \cdot \boldsymbol{u}^- < 0$ for anti-aligned pairs. We compute the resulting solid angle-integrated conditional correlations which we plot in figure 3(*a,b*) normalised by $|\tilde{R}_{12}(y, r)|$, and identify them by ($\rightrightarrows$) for the aligned and ($\rightleftarrows$) for the anti-aligned condition. For both Reynolds numbers and for all wall distances tested, the conditional correlations are increasing functions of r, but positive when the condition is anti-alignment and negative when the condition is alignment. Anti-alignment, which is not so expected within sweeps and ejections (but may be linked to sweep-ejection pairs), increases the magnitude of the
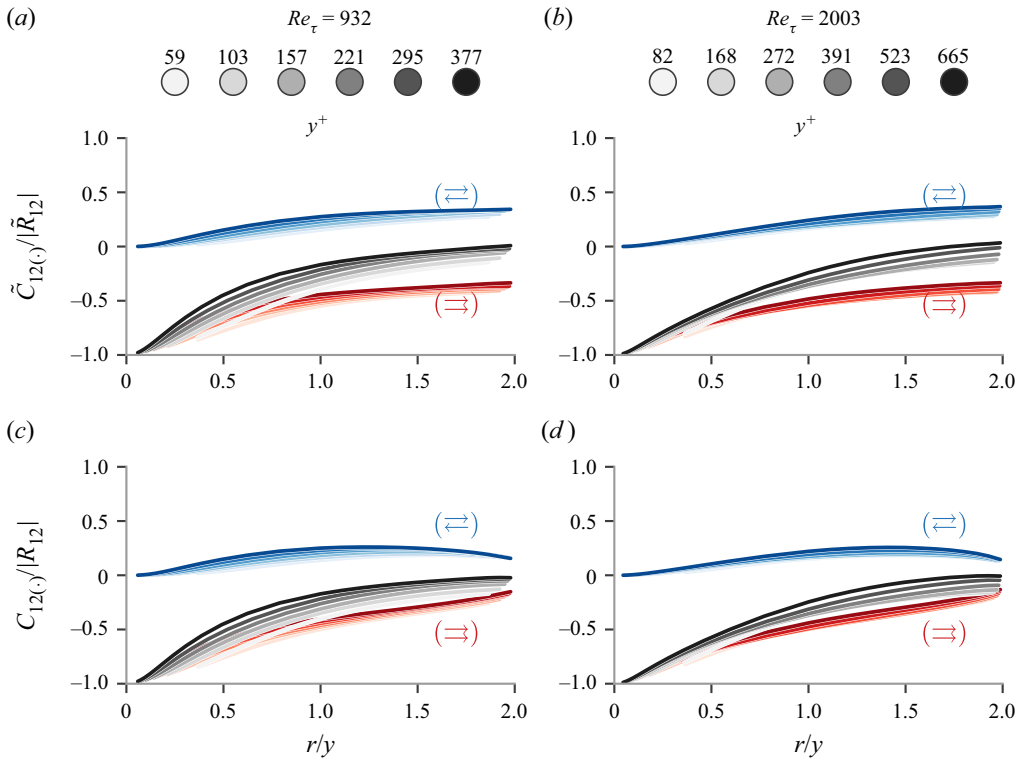
Figure 3. (*a,b*) $\tilde{C}_{12}/|\tilde{R}_{12}|$ integrated over the whole sphere in black lines, conditionally integrated over anti-aligned pairs in blue lines and conditionally integrated over aligned pairs in red lines: (*a*) $Re_\tau = 932$; (*b*) $Re_\tau = 2003$. (*c,d*) Similarly for $C_{12}/|R_{12}|$. Wall-normal distance is increased from light to dark colours as in figure 1.

negative value of $\tilde{S}_{12}(r, y)$, particularly at the larger separations r, whereas alignment, presumably more present within sweeps and ejections, actually contributes to reduce the magnitude of the negative value of $\tilde{S}_{12}(r, y)$. As a result, the part of $-\tilde{S}_{12}(r, y)$ that is conditional on aligned fluctuating velocities is smaller than the part of $-\tilde{S}_{12}(r, y)$ that is conditional on anti-aligned fluctuating velocities, particularly at values of r larger than the Taylor length-scale (see figure 4). The actual role of the Taylor length appears in § 6.

The two-point Reynolds shear stress determines two-point turbulence production via $S_{12}(r, y)$ in the intermediate y-region (see (4.8)). Our results on $\tilde{S}_{12}(r, y)$, $\tilde{R}_{12}(y, r)$ and $\tilde{C}_{12}(r, y)$ and their signs carry over qualitatively to $S_{12}(r, y)$, $R_{12} \equiv 2 \int \langle u_2^+ u_1^+ \rangle [1 - (r_2/2y)^2]^{-1} \, \mathrm{d}\Omega_r$ and $C_{12}(r, y) \equiv 2 \int \langle u_2^+ u_1^- \rangle [1 - (r_2/2y)^2]^{-1} \, \mathrm{d}\Omega_r$ (with differences only at values of r close to $2y$ because of the factor $[1 - (r_2/2y)^2]^{-1}$ in the integrands which tends to infinity for $r_2 \to 2y$, see figures 3(*c,d*) and 4(*c,d*) and compare them respectively with figures 3(*a,b*) and 4(*a,b*)). The two-point turbulence production is therefore positive for all $r \le 2y$ and all y in the intermediate range mainly because one-point turbulence production is positive even though two-point correlations conditioned on aligned fluctuating velocities act to reduce this positivity. Two-point correlations conditioned on anti-aligned fluctuating velocities enhance the positive two-point turbulence production particularly at the larger separations r.
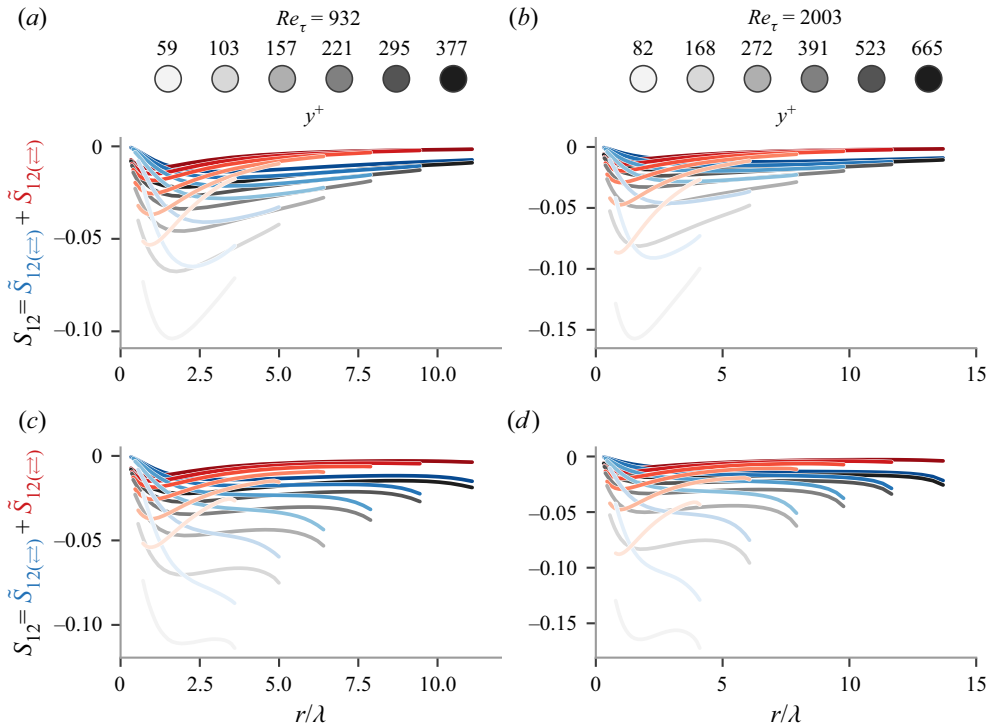
Figure 4. (*a,b*) $\tilde{S}_{12}$ integrated over the whole sphere in black lines, conditionally integrated over anti-aligned pairs in blue lines and conditionally integrated over aligned pairs in red lines: (*a*) $Re_\tau = 932$; (*b*) $Re_\tau = 2003$. (*c,d*) Similarly for S_{12}. Wall-normal distance is increased from light to dark colours as in figure 1. The Taylor length λ is defined in § 6.3.

6. Interscale transfer rate

Having analysed the production term in the scale-by-scale turbulence energy balance (4.1), we now turn our attention to the interscale transfer rate (4.2) and the viscous diffusion terms (4.3). We adapt to the scale-by-scale turbulence energy balance (4.9) (which we derived from (4.1)) the matched asymptotic expansion approach that Lundgren (2002) used to study freely decaying homogeneous isotropic turbulence, a very different flow from FD TCF.

The starting point is the hypothesis that S_2, S_3 and S_{12} have similarity forms, namely,

$$S_2(r, y) = v^2(y)s_2(r/l(y), y), \tag{6.1}$$

$$S_3(r, y) = v^3(y)s_3(r/l(y), y), \tag{6.2}$$

$$S_{12}(r, y) = v^2(y)s_{12}(r/l(y), y), \tag{6.3}$$

in terms of a characteristic velocity v and a characteristic length l both of which depend on wall-normal distance y. In §§ 6.1 and 6.2, this hypothesis is made for small scales $r \ll l_o$ in terms of an inner characteristic velocity $v = v_i$ and an inner characteristic length $l = l_i$, and is also made for large scales $r \gg l_i$ in terms of an outer characteristic velocity $v = v_o$ and outer characteristic length $l = l_o$.

From the one-point balance between average turbulence production $-\langle u_1 u_2 \rangle (dU_1/dy)$ and average turbulence dissipation in the intermediate range $\delta_\nu \ll y \ll \delta$, it is classically claimed, by assuming validity of the log law for the mean flow and its consequence on

967 A22-10

the one-point Reynolds shear stress, that the turbulence dissipation rate equals $u_\tau^3/(\kappa y)$ (e.g. see Pope 2000). Even though there are deviations from both the log law and this dissipation scaling (e.g. Dallas, Vassilicos & Hewitt 2009; Vassilicos *et al.* 2015), we use here the relation $\varepsilon^v = 4u_\tau^3/(\kappa y)$ as an acceptable approximation (in all figures, however, ε^v is computed from the numerical data).

With $\varepsilon^v = 4u_\tau^3/(\kappa y)$ and similarity forms (6.1), (6.2) and (6.3), the balance (4.9) becomes

$$\frac{\kappa}{4}\frac{v^3(y)}{u_\tau^3}\frac{s_3(r/l(y))}{r/y} - \frac{3\kappa y^2}{32\pi r^3 y^+}\int_0^r \rho^2 \frac{d^2\left[\dfrac{v^2(y)}{u_\tau^2}s_2(\rho/l(y))\right]}{dy^2}d\rho$$

$$- \frac{3\kappa y^2}{4\pi ry^+}\frac{d}{dr}\left[\frac{v^2(y)}{u_\tau^2}s_2(r/l(y))\right]$$

$$\approx -1 - \frac{3}{16\pi r^3}\int_0^r \rho^2 \frac{v^2(y)}{u_\tau^2}s_{12}(\rho/l(y))\,d\rho, \tag{6.4}$$

where $y^+ \equiv y/\delta_v = u_\tau y/\nu$ is a naturally appearing local Reynolds number. The functions s_2, s_3 and s_{12} have also explicit dependencies on y in (6.4), (6.5) and (6.10), which are omitted to lighten notation.

In the limit $y^+ \gg 1$ within the intermediate range $\delta_v \ll y \ll \delta$, which of course also requires the limit $Re_\tau = \delta/\delta_v \gg 1$, we consider separately outer similarity with outer variables $v = v_o$ and $l = l_o$ for $r \gg l_i$, and inner similarity with inner variables $v = v_i$ and $l = l_i$ for $r \ll l_o$.

6.1. *Outer similarity*

For r large enough, i.e. $r \gg l_i(y)$ (where the inner length-scale l_i is to be determined), the most natural choice for outer variables is $v = v_o = u_\tau$ and $l = l_o = y$ given that the distance to the wall should somehow determine the size of large eddies and that their characteristic velocity should scale with the skin friction velocity. With these outer variables, (6.4) becomes

$$\frac{\kappa}{4}\frac{s_3(r/y)}{r/y} - \frac{3\kappa y^2}{32\pi r^3 y^+}\int_0^r \rho^2 \frac{d^2[s_2(\rho/y)]}{dy^2}d\rho - \frac{3\kappa y^2}{4\pi ry^+}\frac{d}{dr}[s_2(r/y)]$$

$$\approx -1 - \frac{3}{16\pi r^3}\int_0^r \rho^2 s_{12}(\rho/y)\,d\rho. \tag{6.5}$$

In the limit $y^+ \gg 1$, viscous diffusion (the second and third terms on the left-hand side) tends to 0 as $1/y^+$ compared with the other terms. This equation therefore suggests outer asymptotic expansions in integer powers of $1/y^+$, which means that the outer similarity

functions s_2, s_3 and s_{12} may be approximated as

$$s_2^o(r/y, y^+) = s_2^{o,0} + \frac{1}{y^+} s_2^{o,1} + \cdots \tag{6.6}$$

$$s_3^o(r/y, y^+) = s_3^{o,0} + \frac{1}{y^+} s_3^{o,1} + \cdots \tag{6.7}$$

$$s_{12}^o(r/y, y^+) = s_{12}^{o,0} + \frac{1}{y^+} s_{12}^{o,1} + \cdots \tag{6.8}$$

with leading orders obeying

$$\frac{\kappa}{4} \frac{s_3^{o,0}(r/y)}{r/y} \approx -1 - \frac{3}{16\pi r^3} \int_0^r \rho^2 s_{12}^{o,0}(\rho/y) \, \mathrm{d}\rho. \tag{6.9}$$

The leading order outer scale-by-scale energy balance is therefore a balance between interscale transfer, turbulence dissipation and two-point turbulence production. (Turbulence dissipation appears in this outer balance essentially because the scale-by-scale energy balance that we consider concerns the sphere-averaged second-order structure function which is cumulative with increasing r.)

6.2. *Inner similarity*

For r small enough, i.e. $r \ll l_o = y$, we seek inner variables of the form $v_i^2 = v_o^2 (1/y^+)^a = u_\tau^2 (1/y^+)^a$ and $l_i = l_o (1/y^+)^b = y(1/y^+)^b$, where the exponents a, b are positive because inner variables should tend to 0 relative to outer ones in the limit where the local Reynolds number y^+ tends to infinity. With such variables, (6.4) becomes

$$\frac{\kappa}{4} \left(\frac{1}{y^+} \right)^{3a/2-b} \frac{s_3(r/l_i)}{r/l_i} - O\left[\left(\frac{1}{y^+} \right)^{a+3-2b} \right] - \frac{3\kappa}{4\pi} \left(\frac{1}{y^+} \right)^{a+1-2b} \frac{s_2'(r/l_i)}{r/l_i}$$

$$\approx -1 - \frac{3}{16\pi r^3} \int_0^r \rho^2 \left(\frac{1}{y^+} \right)^a s_{12}(\rho/l_i) \, \mathrm{d}\rho, \tag{6.10}$$

where $s_2'(r/l_i)$ is the derivative of s_2 with respect to r/l_i. In the limit $y^+ \gg 1$, the two-point turbulence production rate tends to 0 as $(1/y^+)^a$ compared with the dissipation rate which is represented in this equation by -1 on the right-hand side. At inner scales, the leading order scale-by-scale turbulence energy balance must therefore involve interscale energy transfer and viscous diffusion to balance dissipation, which implies $(3a/2) - b = 0 = a + 1 - 2b$ and therefore $a = 1/2$ and $b = 3/4$. In the limit $y^+ \to \infty$, i.e. $y^+ \gg 1$, this equation therefore suggests inner asymptotic expansions in integer powers of $(1/y^+)^a = (1/y^+)^{1/2}$, which means that the inner similarity functions s_2, s_3 and s_{12} may

967 A22-12

be approximated as

$$s_2^i(r/l_i, y^+) = s_2^{i,0} + \left(\frac{1}{y^+}\right)^{1/2} s_2^{i,1} + \cdots, \tag{6.11}$$

$$s_3^i(r/l_i, y^+) = s_3^{i,0} + \left(\frac{1}{y^+}\right)^{1/2} s_3^{i,1} + \cdots, \tag{6.12}$$

$$s_{12}^i(r/l_i, y^+) = s_{12}^{i,0} + \left(\frac{1}{y^+}\right)^{1/2} s_{12}^{i,1} + \cdots \tag{6.13}$$

with leading orders obeying

$$\frac{\kappa}{4} \frac{s_3^{i,0}(r/l_i)}{r/l_i} \approx -1 - \frac{3\kappa}{4\pi} s_2^{i,0'}(r/l_i), \tag{6.14}$$

where $s_2^{i,0'}(r/l_i)$ is the derivative of $s_2^{i,0}$ with respect to r/l_i. The leading order inner scale-by-scale energy balance is therefore a balance between interscale transfer, turbulence dissipation and viscous diffusion.

The values $a = 1/2$ and $b = 3/4$ that we derived imply that the inner variables are in fact Kolmogorov inner variables, i.e. $v_i = u_\eta \equiv (\nu\varepsilon^v)^{1/4}$ and $l_i = \eta \equiv (\nu^3/\varepsilon^v)^{1/4}$ (using $\varepsilon^v = u_\tau^3/(\kappa y)$).

6.3. *Intermediate matching*

Starting with the second-order structure function S_2, matching the leading term $u_\tau^2 s_2^{o,0}(r/y)$ of its outer expansion for $r \gg \eta$ with the leading term $u_\tau^2 (1/y^+)^{1/2} s_2^{i,0}(r/\eta)$ of its inner expansion for $r \ll y$ leads to

$$S_2^0 \sim (\varepsilon^v r)^{2/3} \tag{6.15}$$

as the overlapping part of the leading order in the intermediate range $\eta \ll r \ll y$.

Similarly,

$$S_{12}^0 \sim (\varepsilon^v r)^{2/3} \tag{6.16}$$

is the overlapping part of the leading order in the intermediate range $\eta \ll r \ll y$ for S_{12}.

It may be interesting to note, in passing, the difference compared to turbulence non-homogeneities with negligible turbulence production but non-negligible spatial turbulence transport, such as in certain turbulent wake regions where Chen & Vassilicos (2022) have shown that a second-order structure function scales as $\sim K(r/L)^{2/3}$, where K is the one-point kinetic energy, L is an integral length scale and turbulence dissipation does not scale as $K^{3/2}/L$. Note that the $K^{3/2}/L$ scaling is effectively the scaling assumed here for ε^v because, in the range $\delta_\nu \ll y \ll \delta$ considered here, the turbulent kinetic energy scales as u_τ^2 plus logarithmic corrections in y (see Townsend 1976; Dallas *et al.* 2009) which we neglect, and because there are integral length scales in FD TCF which are proportional to y, see Apostolidis *et al.* (2022). The types of non-homogeneity considered by Chen & Vassilicos (2022) are opposite to those considered here where spatial turbulence transport is negligible but turbulence production is not.

To obtain the leading order of S_3, and therefore of the interscale transfer rate Π^v via (4.2), we use (6.9) and (6.14). From the leading order outer balance, (6.9) follows

$$S_3^{o,0} \approx -\varepsilon^v r(1 - A(r/y)^{2/3}), \qquad (6.17)$$

where A is a dimensionless constant, and from the leading order inner balance, (6.14) follows

$$S_3^{i,0} \approx -\varepsilon^v r(1 - B(r/\eta)^{-4/3}), \qquad (6.18)$$

where B is another dimensionless constant. The composite leading order (see Van Dyke 1964; Cole 1968; Hinch 1991) written directly for the interscale transfer $\Pi^v = S_3/r$ is $S_3^{o,0}/r$ plus $S_3^{i,0}/r$ minus their common part $-\varepsilon^v$, i.e.

$$\Pi^v \approx -\varepsilon^v(1 - A(r/y)^{2/3} - B(r/\eta)^{-4/3}), \qquad (6.19)$$

where we now omit superscripts for ease of notation.

This last equation has the following two verifiable implications, both of which are relatively easy to verify with the DNS data at our disposal. First, it implies that the value of r where Π^v/ε^v is minimal and closest to the Kolmogorov equilibrium value -1 is

$$r_{min} \sim \sqrt{\delta_\nu y} \sim \lambda \qquad (6.20)$$

based on the definition $\lambda^2 \equiv 10\nu K/\varepsilon$ (already used by Dallas *et al.* (2009) in the context of FD TCF), and on $K \sim u_\tau^2$ and $\varepsilon \sim u_\tau^3/y$ being good enough approximations in the present context for $\delta_\nu \ll y \ll \delta$. Conclusions such as (6.19) and (6.20) have recently been obtained by Zimmerman *et al.* (2022) for the centreline of FD TCF and central axis of turbulent pipe flow where turbulence production is effectively absent.

Second, (6.19) also implies that the value $(\Pi^v/\varepsilon^v)_{min}$ of Π^v/ε^v at $r = r_{min}$ obeys

$$1 + (\Pi^v/\varepsilon^v)_{min} \sim y^{+^{-1/3}} \sim Re_\lambda^{-2/3}, \qquad (6.21)$$

where $Re_\lambda = \sqrt{K}\lambda/\nu$. Consistent with our averages over spheres in r-space, these definitions of λ and Re_λ ignore some anisotropies of FD TCF. It is possible to define different Taylor lengths for different directions so as to take explicit account of anisotropies, which is an approach we have taken in another study (Yuvaraj 2022). It may be noteworthy that the Corrsin length (Sagaut & Cambon 2018) does not appear spontaneously from our analysis, whereas the Kolmogorov and Taylor lengths do. The reason for this absence of the Corrsin length is that it equals κy at the approximation level of our theory in the intermediate layer $\delta_\nu \ll y \ll \delta$ and is therefore comparable to the outer bound of the range $r \leq 2y$ considered here.

In conclusion, the non-homogeneous but statistically stationary case of FD TCF in the intermediate layer $\delta_\nu \ll y \ll \delta$ is such that Kolmogorov equilibrium is achieved asymptotically around λ and therefore not quite in an inertial range given that λ depends on viscosity, and that there is a systematic departure from equilibrium when moving away from λ, both towards L and towards η, see (6.19). (Note, however, that the non-zero deviation from Kolmogorov equilibrium as Reynolds number tends to infinity for a fixed small value of r/y or for a fixed large value of r/η (necessarily smaller than λ/η in the limit) is small.) This is the same conclusion that the analysis of Lundgren (2002) reached for freely decaying, i.e. non-stationary, but statistically homogeneous and isotropic turbulence far from initial conditions. Two-point turbulence production (which increases with r as confirmed in the following section) and its variation with wall-normal distance play a similar role in FD TCF as the rate of decay of the second-order velocity structure function (which increases with r because unsteadiness increases with r) and its variation with time.
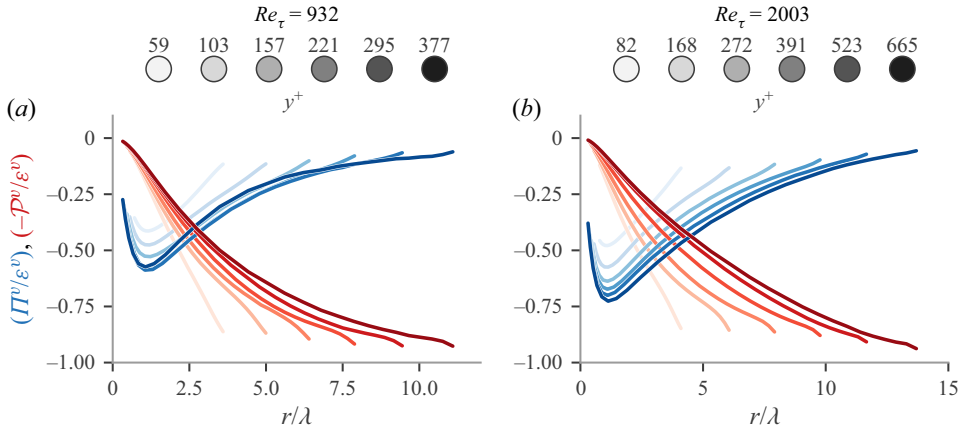
Figure 5. Interscale transfer rate Π (blue lines) and production rate $\mathcal{P}$ (red lines), integrated over the volume of sphere with radius r, normalised by the volume integral of the two-point dissipation rate ε as a function of r/λ. Wall-normal distance is increased from light to dark colours. (*a*) For $Re_\tau = 932$ and (*b*) for $Re_\tau = 2003$.

7. Comparison with DNS data for FD TCF

In this section, we compare the theory of the previous sections with the DNS data described in § 3.

In figure 5(*a*,*b*), we plot the two-point turbulence production rate $\mathcal{P}^v$ and the interscale transfer rate Π^v, both normalised by the turbulence dissipation rate ε^v. We plot them vs r/λ because of our prediction that the value of r, where Π^v/ε^v is minimal, scales with λ. The maximum values of r in the plots are bounded by $2y$ because of wall-blocking. We see that the normalised two-point turbulence production rate $\mathcal{P}^v/\varepsilon^v$ increases from close to 0 to a little under 1 as r increases from 0 to $2y$. This is evidenced for a wide range of wall-normal distances y and for both Reynolds numbers at our disposal. It makes sense that the two-point turbulence production acts as a generation of turbulent kinetic energy at the larger r scales but decreasingly so at smaller and smaller scales till it vanishes at the very smallest ones.

It is also clear from figure 5(*a*,*b*) that Π^v is negative for all scales and wall distances, indicating a forward, on average, energy cascade for $r < 2y$. Furthermore, Π^v/ε^v has a minimum at r_{min} close to λ for a wide range of y within $\delta_v \ll y \ll \delta$ and for both Reynolds numbers. This confirms our prediction (6.20) as can be seen in figure 6(*a*) where we plot, in blue, r_{min}/λ vs y^+ for both Reynolds numbers and find that $r_{min} \approx 1.2\lambda$. One also sees in figure 5(*a*,*b*) that $(\Pi^v/\varepsilon^v)_{min}$ increases in magnitude with increasing y^+ and with increasing Re_τ. This is confirmed in figure 6(*b*) where we plot, in blue, $1 + (\Pi^v/\varepsilon^v)_{min}$ vs Re_λ confirming that $-(\Pi^v/\varepsilon^v)_{min}$ increases towards 1 following our prediction 6.21, which collapses both the y^+ and the Re_τ dependencies of $-(\Pi^v/\varepsilon^v)_{min}$. Note, in passing, that the values of Re_λ are not so high for the present Re_τ values of approximately 1000 to 2000: they range from approximately 50 to 120 (and in fact reach no more than a maximum of 200 at the outer edge of the intermediate y-range if Re_τ is pushed up to 5200 as Apostolidis *et al.* 2022 also found).

The imbalance seen in figure 5 between Π^v and ε^v is a clear indication that other processes in the scale-by-scale energy budget are active. The theoretical arguments of §§ 6.1 and 6.2 concluded that the scale-by-scale balance is approximately $\Pi^v - \mathcal{P}^v \approx -\varepsilon^v$ at the outer scales and $\Pi^v - D_r^v \approx -\varepsilon^v$ at the inner scales. This prediction is made in the
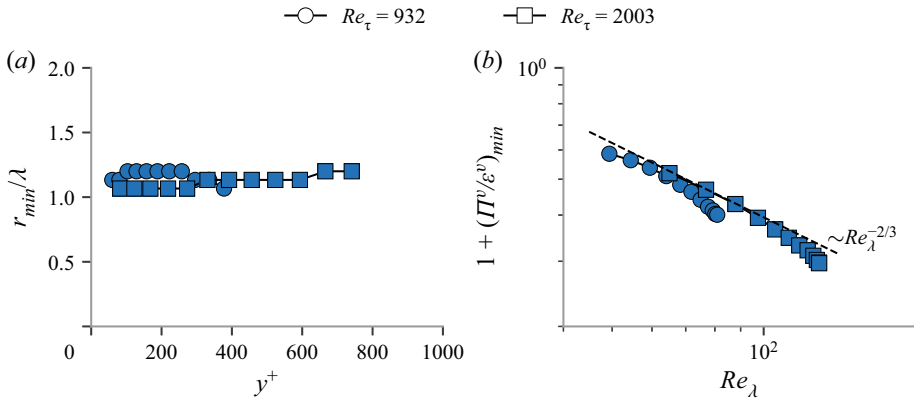
Figure 6. (*a*) Values of r/λ where minima of Π^v/ε^v are observed as a function of wall distance y^+. (*b*) Values of $1 + (\Pi^v/\varepsilon^v)_{min}$, in blue, as a function of Re_λ. Dashed line shows a scaling of $Re_\lambda^{-2/3}$. Circle markers for $Re_\tau = 932$; square markers for $Re_\tau = 2003$.
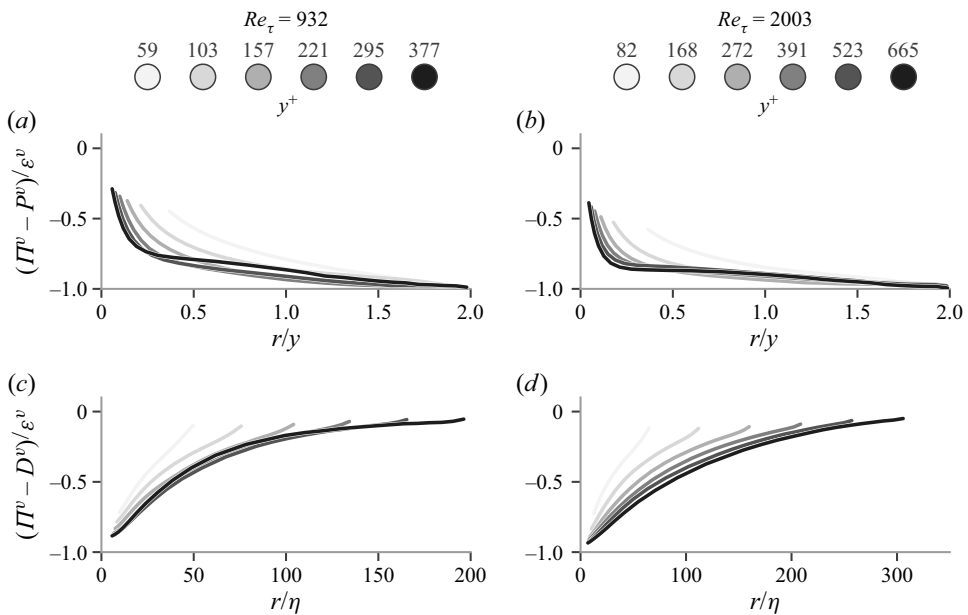

Figure 7. (*a,b*) $(\Pi^v - \mathcal{P}^v)/\varepsilon^v$ as a function of r/y: (*a*) for $Re_\tau = 932$ and (*b*) for $Re_\tau = 2003$. (*c,d*) $(\Pi^v - D^v)/\varepsilon^v$ as a function of r/η: (*c*) for $Re_\tau = 932$ and (*d*) for $Re_\tau = 2003$. Wall-normal distance is increased from light to dark colours.

limit $Re_\tau = \delta/\delta_v \gg 1$ and $\delta_v \ll y \ll \delta$ and, as the values of Re_λ suggest, the Reynolds numbers in the DNS data we are using may not be high enough. Nevertheless, figure 7(*a,b*) does reveal some tendency for $(\Pi^v - \mathcal{P}^v)/\varepsilon^v$ to collapse as a function of r/y and tend towards -1 at the higher values of r/y as y^+ grows, in particular for the higher of our two Reynolds numbers Re_τ. Furthermore, figure 7(*c,d*) reveals some tendency for $(\Pi^v - D_r^v)/\varepsilon^v$ to collapse as a function of r/η as y^+ grows and even to tend towards -1 at the smallest values of r/η.

967 A22-16
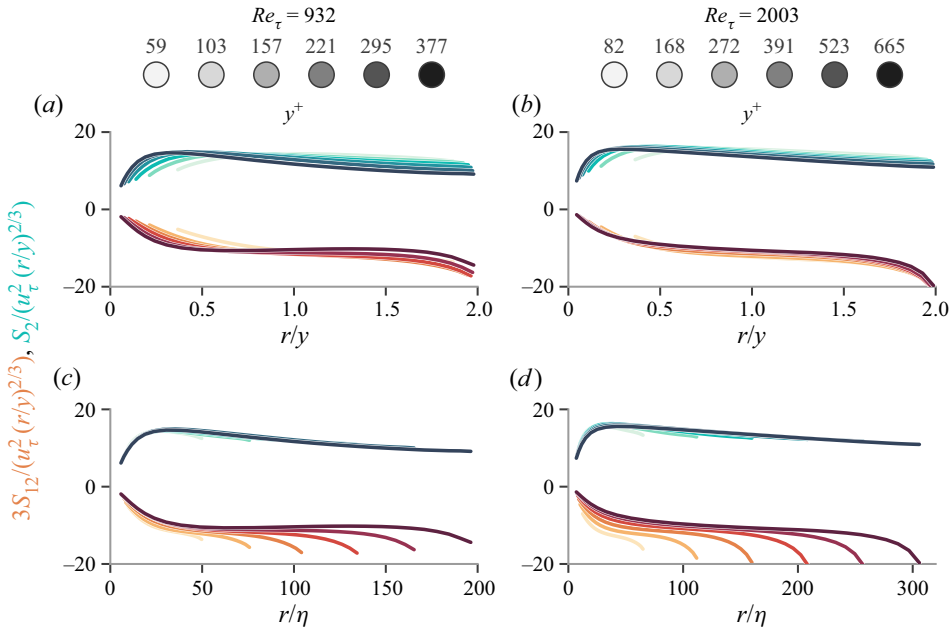
Figure 8. S_{12} in orange colours (multiplied by a factor of 3 for ease of comparison) and S_2 in marine colours normalised with $u_\tau^2(r/y)^{2/3}$ as a function of (a,b) r/y and of (c,d) r/η: (a,c) for $Re_\tau = 932$; (b,d) for $Re_\tau = 2003$. Wall-normal distance is increased from light to dark colours.

Finally, we compare the high-Reynolds-number predictions (6.15), (6.16) and (6.19) with the DNS data. In figure 8(a,b), we plot $S_2/u_\tau^2(r/y)^{2/3}$ and $S_{12}/u_\tau^2(r/y)^{2/3}$ vs r/y to test outer scalings and in figure 8(c,d), we plot the same quantities vs r/η to test inner scalings. Note that we use u_τ^3/y as an estimate of ε^v. Our DNS data lend more support to our $r^{2/3}$ prediction for S_{12} than for S_2, and a better outer collapse in terms of r/y of $S_{12}/u_\tau^2(r/y)^{2/3}$ than $S_2/u_\tau^2(r/y)^{2/3}$. However, the inner collapse in terms of r/η appears better for $S_2/u_\tau^2(r/y)^{2/3}$ than $S_{12}/u_\tau^2(r/y)^{2/3}$. At any rate, the values of Re_λ are quite low in the DNS data used here for a conclusive comparison between these data and theoretical predictions made in the double limit $Re_\tau \to \infty$, $y^+ \to \infty$ (i.e. $Re_\lambda \sim \lambda/\delta_v \sim (y^+)^{1/2} \to \infty$) with the constraint $y \ll \delta$. In fact, even at the very lowest/leading order, our predictions (6.15), (6.16) are incomplete as they should have corrections in terms of powers of r/η and r/y which are beyond the present theory and which surely matter in comparisons with DNS data.

We close this section with a comparison in figure 9 of (6.19) with the DNS data which is clearly better for $Re_\tau = 2003$ than $Re_\tau = 932$.

8. Interscale transfer decompositions

The two main conclusions of the previous sections concern (i) the importance of the Taylor length in defining the scale where the normalised interscale transfer rate Π^v/ε^v has a minimum and is closest to the equilibrium value $\Pi^v/\varepsilon^v = -1$ and (ii) the importance of sweeps and ejections but also of aligned and anti-aligned pairs of fluctuating velocities in determining the sign and magnitude of the two-point turbulence production rate $\mathcal{P}^v$.
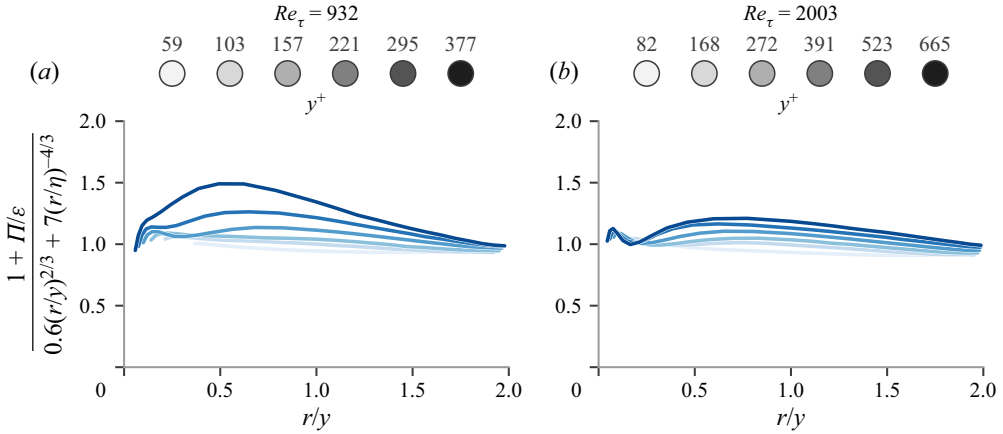
Figure 9. Rearrangement of (6.19) vs r/y: (*a*) for $Re_\tau = 932$; (*b*) for $Re_\tau = 2003$. Wall-normal distance is increased from light to dark colours.

Looking at (4.2), we start this section by asking whether aligned and anti-aligned pairs of fluctuating velocities also directly affect the interscale transfer rate Π^v.

8.1. *Aligned/anti-aligned decomposition*

Equation (4.2) shows that a scale-space flux and a cascade from large to small or from small to large scales correspond to a negative or positive $(3/4\pi)\int\langle(\hat{\boldsymbol{r}}\cdot\delta\boldsymbol{u}/r)|\delta\boldsymbol{u}|^2\rangle\,\mathrm{d}\Omega_{\boldsymbol{r}}$ and contributes a growth or decrease of TKE at scales r and smaller (see Chen & Vassilicos 2022). Local compression, i.e. $\delta\boldsymbol{u}\cdot\hat{r} < 0$, causes local forward cascade and local stretching, i.e. $\delta\boldsymbol{u}\cdot\hat{r} > 0$, causes local inverse cascade. Our observation that Π^v is negative at all scales means that local compressions prevail at all scales, but are they mostly caused by aligned or anti-aligned pairs of fluctuating velocities? This question introduces our first decomposition, namely

$$\Pi^v = \Pi^v_{\rightrightarrows} + \Pi^v_{\rightleftarrows} = \frac{3}{4\pi}\int\left\langle\frac{\delta\boldsymbol{u}\cdot\hat{\boldsymbol{r}}}{r}|\delta\boldsymbol{u}|^2\right\rangle_{\rightrightarrows}\mathrm{d}\Omega_r + \frac{3}{4\pi}\int\left\langle\frac{\delta\boldsymbol{u}\cdot\hat{\boldsymbol{r}}}{r}|\delta\boldsymbol{u}|^2\right\rangle_{\rightleftarrows}\mathrm{d}\Omega_r, \quad (8.1)$$

where $\Pi^v_{\rightrightarrows}$ and $\Pi^v_{\rightleftarrows}$ are respectively equal to the first and second terms on the left-hand side which are calculated using averages $\langle\cdots\rangle_{\rightrightarrows}$ conditional on $\boldsymbol{u}^+\cdot\boldsymbol{u}^- > 0$ and averages $\langle\cdots\rangle_{\rightleftarrows}$ conditional on $\boldsymbol{u}^+\cdot\boldsymbol{u}^- < 0$.

Compressive and stretching relative motions may not balance in terms of energy transfer, resulting in a non-vanishing Π^v, but they do balance in terms of mass transfer because of incompressibility which implies $\int\delta\boldsymbol{u}\cdot\hat{r}\,\mathrm{d}\Omega_r = 0$. Hence,

$$\int\langle\delta\boldsymbol{u}\cdot\hat{\boldsymbol{r}}\rangle_{\rightrightarrows}\mathrm{d}\Omega_r + \int\langle\delta\boldsymbol{u}\cdot\hat{\boldsymbol{r}}\rangle_{\rightleftarrows}\mathrm{d}\Omega_r = 0. \tag{8.2}$$

In figure 10, we plot both terms on the left-hand side of this equation as functions of r for various wall distances y. We also plot $\int\delta\boldsymbol{u}\cdot\hat{r}\,\mathrm{d}\Omega_r$ for comparison and as a check that it is indeed zero in the DNS irrespective of r and y. The first observation is that aligned fluctuation pairs are stretching relative motions on average given the positive sign of $\int\langle\delta\boldsymbol{u}\cdot\hat{\boldsymbol{r}}\rangle_{\rightrightarrows}\mathrm{d}\Omega_r$. The joint PDFs of figure 11 show that relative motions of aligned fluctuation pairs are stretching as a result of $\delta\boldsymbol{u}$ having a tendency to be directed in the same

967 A22-18
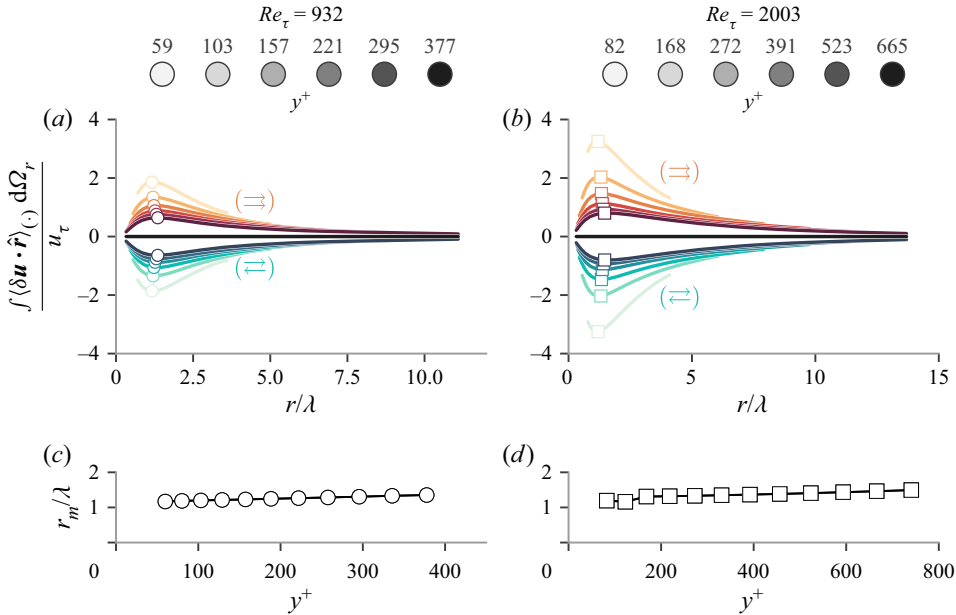
Figure 10. $\int \langle \delta\boldsymbol{u} \cdot \hat{\boldsymbol{r}} \rangle \mathrm{d}\Omega_r$ integrated over the whole sphere in black lines, conditionally integrated over anti-aligned pairs in marine colours, and conditionally integrated over aligned pairs in orange colours. Wall-normal distance is increased from light to dark colours. (*a*) $Re_\tau = 932$, (*b*) $Re_\tau = 2003$. (*c*) r/λ positions of the minima/maxima observed in panel (*a*) as a function of wall-distance y^+ for $Re_\tau = 932$, similarly in panel (*d*) for $Re_\tau = 2003$.

direction as the separation vector $\boldsymbol{r}$ for pairs of aligned fluctuating velocities. This tendency weakens with increasing r irrespective of wall distance y and, consistently, $\int \langle \delta\boldsymbol{u} \cdot \hat{\boldsymbol{r}} \rangle_{\rightrightarrows} \mathrm{d}\Omega_r$ tends to 0 with increasing r.

The second observation in figure 10 is that anti-aligned fluctuation pairs are compressing relative motions, on average, given the negative sign of $\int \langle \delta\boldsymbol{u} \cdot \hat{\boldsymbol{r}} \rangle_{\rightleftarrows} \mathrm{d}\Omega_r$. Looking at figure 11, it does not seem possible to explain this behaviour purely in terms of velocity directions. However, the joint PDFs of figure 12 reveal that the range of values over which $\delta\boldsymbol{u} \cdot \hat{\boldsymbol{r}}$ fluctuates around zero is much wider for anti-aligned than for aligned fluctuations. This effect has to do with the intensity of the fluctuating velocities, not only their relative directions. This very wide fluctuation range is slightly skewed towards negative values of $\delta\boldsymbol{u} \cdot \hat{\boldsymbol{r}}$ for pairs of fluctuating velocities which are anti-aligned, thereby accounting for the compressive average behaviour of anti-aligned pairs ($\boldsymbol{u}^+ \cdot \boldsymbol{u}^- < 0$). This skewness diminishes with increasing r irrespective of wall distance y and, consistently, $\int \langle \delta\boldsymbol{u} \cdot \hat{\boldsymbol{r}} \rangle_{\rightleftarrows} \mathrm{d}\Omega_r$ tends to 0 with increasing r. Note, finally, that it is far more likely to find aligned ($\boldsymbol{u}^+ \cdot \boldsymbol{u}^- > 0$) than anti-aligned ($\boldsymbol{u}^+ \cdot \boldsymbol{u}^- < 0$) pairs as figure 11 shows.

The third observation in figure 10 is that $\int \langle \delta\boldsymbol{u} \cdot \hat{\boldsymbol{r}} \rangle_{\rightleftarrows} \mathrm{d}\Omega_r$ has a minimum at $r = r_m$ near $r_{min} \approx 1.2\lambda$ for all y and that $\int \langle \delta\boldsymbol{u} \cdot \hat{\boldsymbol{r}} \rangle_{\rightrightarrows} \mathrm{d}\Omega_r$ has a maximum at the same value $r = r_m$ for all y. As seen in the previous two sections, r_{min} is the value of r where Π^v/ε^v has its minimum. In figure 10(*c,d*), we plot the positions r of the maxima and minima in figure 10 vs wall distance for both DNS Reynolds numbers at our disposal. It is quite striking that, for all wall distances and both Reynolds numbers tried, $\int \langle \delta\boldsymbol{u} \cdot \hat{\boldsymbol{r}} \rangle_{\rightleftarrows} \mathrm{d}\Omega_r$ and $\int \langle \delta\boldsymbol{u} \cdot \hat{\boldsymbol{r}} \rangle_{\rightrightarrows} \mathrm{d}\Omega_r$ peak at $r = r_m$ close to the value $r = r_{min}$, where Π^v/ε^v peaks and is closest to the equilibrium -1 value. Even though r_m drifts slightly from $r_{min} \approx 1.2\lambda$ at relatively high wall-normal distances, the suggestion is that, in the layer $\delta_v \ll y \ll \delta$ of FD
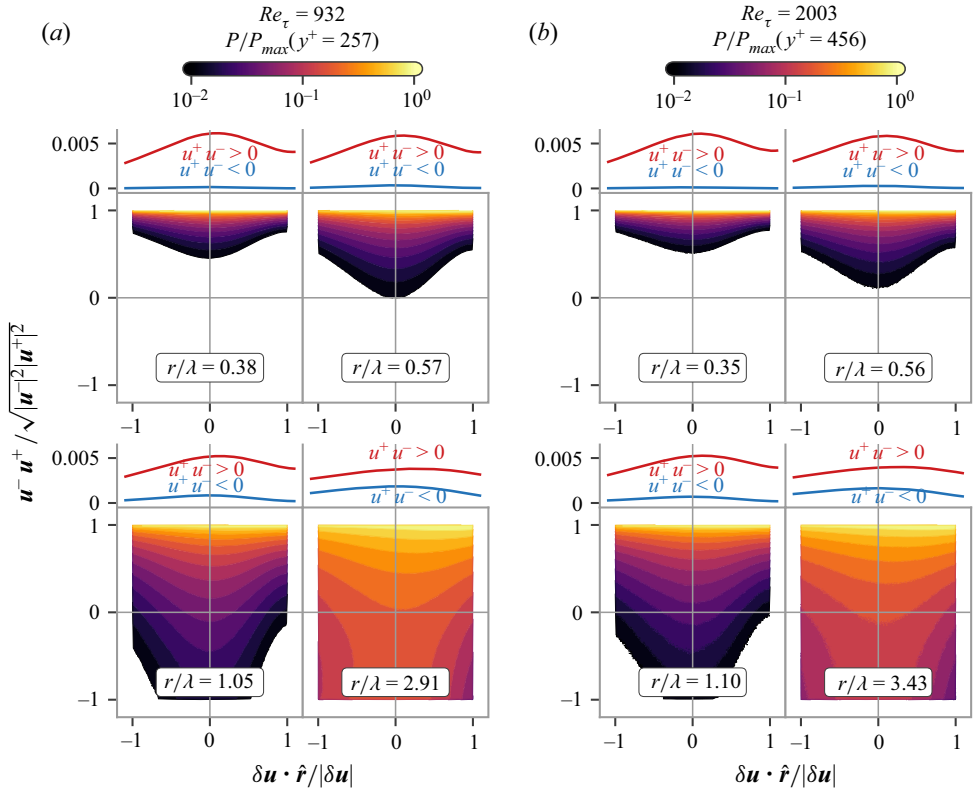
Figure 12. Joint probability distribution functions (JPDFs) of $\delta\boldsymbol{u}\cdot\hat{\boldsymbol{r}}$ and $\boldsymbol{u}^{-}\boldsymbol{u}^{+}$. (a) For $Re_{\tau} = 932$ and wall-distance $y^{+} = 257$, four different JPDFs with increasing scale $r/\lambda = 0.38, 0.57, 1.05$ and 2.91. (b) Similarly for $Re_{\tau} = 2003$ and wall-distance $y^{+} = 456$, the JPDFs correspond to scales $r/\lambda = 0.35, 0.56, 1.10$ and 3.43. The joint PDFs are normalised with their maximum value, while the values of the x and y axis are normalised with their own standard deviations.
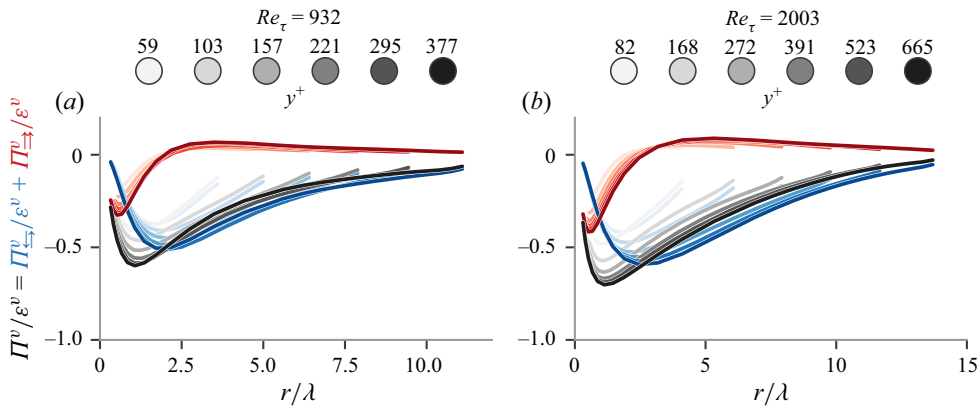

Figure 13. Decomposition of the interscale transfer term Π^{v} (black lines) into $\Pi_{\rightleftarrows}^{v}$ (blue lines) and $\Pi_{\rightrightarrows}^{v}$ (red lines): (a) $Re_{\tau} = 932$; (b) $Re_{\tau} = 2003$. Wall-normal distance is increased from light to dark colours.

Aligned fluctuation pairs impose a loss of energy on scales smaller than r by mean flow interaction with turbulence fluctuations and thereby reduce the one-point effect of sweeps and ejections on the two-point turbulence production rate (see § 5). We have now seen that aligned fluctuation pairs are on average stretching, which would suggest the presence of an average inverse cascade element to the interscale transfer rate $\Pi_{\rightrightarrows}^{v}$. Figure 13 shows that $\Pi_{\rightrightarrows}^{v}$ is positive (though only slightly so), and an average inverse cascade by aligned fluctuations is indeed present at scales r larger than approximately 2 to 3 times λ for the Reynolds numbers of the DNS data used here. However, figure 13 also shows that $\Pi_{\rightrightarrows}^{v}$ is

967 A22-21

negative at smaller scales. Stretching aligned fluctuating motions at scales of the order of the Taylor length and below may dominate over compressive aligned fluctuating motions, on average, but they do not dominate interscale energy transfer at these scales. There is no contradiction with the positive values of $\int \langle \delta \boldsymbol{u} \cdot \hat{\boldsymbol{r}} \rangle_{\rightrightarrows} \, \mathrm{d}\Omega_r$ in figure 10. The different signs of this solid angle integral and the solid angle integral in the definition of $\Pi^v_{\rightrightarrows}$ (see (8.1)) are an effect of small-scale anisotropies over which we are averaging. Future studies of interscale transfers in FD TCFs will need to take these anisotropies into account for a finer description of the physics.

Finally, comparing the plots of Π^v in figure 5 with those of $\Pi^v_{\rightrightarrows}$ and $\Pi^v_{\rightleftarrows}$ in figure 13 shows that $\Pi^v_{\rightleftarrows}$ dominates over $\Pi^v_{\rightrightarrows}$ at scales of the order of λ and larger, and is mostly responsible for the value of Π^v. At smaller scales, however, $\Pi^v_{\rightrightarrows}$ becomes equally important and of the same negative sign as $\Pi^v_{\rightleftarrows}$ so that the actual negative value of Π^v cannot be accounted for by only one or the other: the interscale turbulence energy transfers of both aligned and anti-aligned fluctuations matter.

8.2. *Homogeneous/Inhomogeneous energy transfer decomposition*

As already mentioned at the start of § 8.1, the right-hand side $(3/4\pi) \int \langle (\hat{\boldsymbol{r}} \cdot \delta \boldsymbol{u}/r) |\delta \boldsymbol{u}|^2 \rangle \mathrm{d}\Omega_r$ of (4.2) shows that local compression, i.e. $\delta \boldsymbol{u} \cdot \hat{\boldsymbol{r}} < 0$, causes local forward cascade, whereas local stretching, i.e. $\delta \boldsymbol{u} \cdot \hat{\boldsymbol{r}} > 0$, causes local inverse cascade (see also § 2 of Chen & Vassilicos 2022). These compressions and stretches may be caused either by turbulence inhomogeneities or by correlated 'eddy' motions. In an attempt to formalise this distinction, Alves Portela, Papadakis & Vassilicos (2020) decomposed the interscale energy transfer rate $\Pi = (\partial/\partial r_i)(\delta u_i |\delta \boldsymbol{u}|^2)$ as follows:

$$\frac{\partial}{\partial r_i}(\delta u_i |\delta \boldsymbol{u}|^2) = \frac{\partial}{\partial r_i}[\delta u_i(|\boldsymbol{u}^+|^2 + |\boldsymbol{u}^-|^2)] - 2\frac{\partial}{\partial r_i}(\delta u_i \boldsymbol{u}^- \cdot \boldsymbol{u}^+), \tag{8.3}$$

where the first term on the right-hand side can be rigorously recast into a gradient in centroid $\boldsymbol{x}$-space leading to

$$\frac{\partial}{\partial r_i}(\delta u_i |\delta \boldsymbol{u}|^2) = \frac{1}{2}\frac{\partial}{\partial x_i}[u_i^+|\boldsymbol{u}^+|^2 + u_i^-|\boldsymbol{u}^-|^2 - u_i^-|\boldsymbol{u}^+|^2 - u_i^+|\boldsymbol{u}^-|^2]$$
$$- 2\frac{\partial}{\partial r_i}(\delta u_i \boldsymbol{u}^- \cdot \boldsymbol{u}^+). \tag{8.4}$$

Here, $\Pi_I \equiv \frac{1}{2}(\partial/\partial x_i)[u_i^+|\boldsymbol{u}^+|^2 + u_i^-|\boldsymbol{u}^-|^2 - u_i^-|\boldsymbol{u}^+|^2 - u_i^+|\boldsymbol{u}^-|^2]$ is interpreted as an inhomogeneity-related interscale turbulent energy transfer rate. In statistically homogeneous turbulence, the average $\langle \Pi_I \rangle$ is indeed zero and the interscale turbulent energy transfer rate is only accountable to $\Pi_H \equiv -2(\partial/\partial r_i)(\delta u_i \boldsymbol{u}^- \cdot \boldsymbol{u}^+)$ on average.

Integrating Π, Π_I and Π_H over the sphere of radius r in $\boldsymbol{r}$-space to obtain Π^v, Π^v_I and Π^v_H, respectively, and then applying the Gauss divergence theorem, we obtain

$$\Pi^v = \Pi^v_I + \Pi^v_H = \frac{3}{4\pi}\left(\int \left\langle \frac{\delta \boldsymbol{u} \cdot \hat{\boldsymbol{r}}}{r}(|\boldsymbol{u}^+|^2 + |\boldsymbol{u}^-|^2)\right\rangle \mathrm{d}\Omega_r \right.$$
$$\left. - 2\int \left\langle \frac{\delta \boldsymbol{u} \cdot \hat{\boldsymbol{r}}}{r}(\boldsymbol{u}^- \cdot \boldsymbol{u}^+)\right\rangle \mathrm{d}\Omega_r\right). \tag{8.5}$$

This decomposition is partly related to that in § 8.1 because Π^v_H is linearly dependent on correlations between $\delta \boldsymbol{u} \cdot \hat{\boldsymbol{r}}$ and $\boldsymbol{u}^- \cdot \boldsymbol{u}^+$, and the sign of $\boldsymbol{u}^- \cdot \boldsymbol{u}^+$ indicates whether velocity
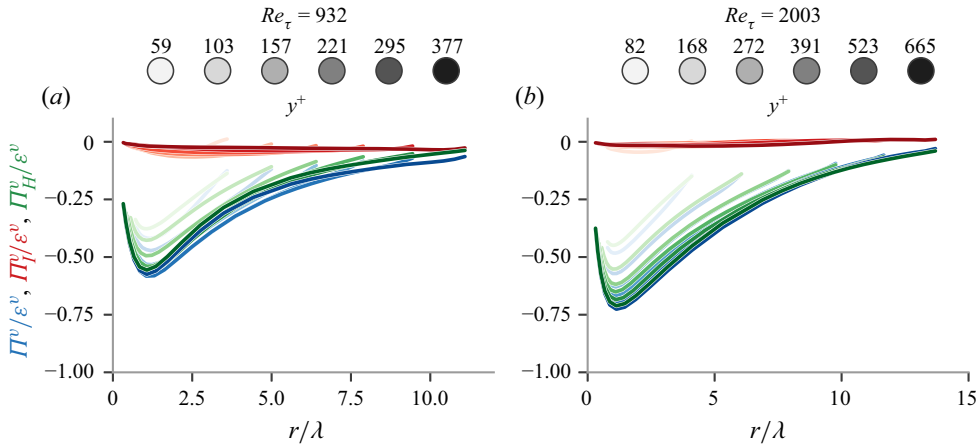
Figure 14. Interscale transfer rate (blue lines), inhomogeneous part Π_I^v (red lines) and homogeneous part Π_H^v (green lines), all integrated over the volume of a sphere and normalised by the dissipation rate integrated over the volume of the sphere as a function of r/λ. Wall-normal distance is increased from light to dark colours. (*a*) For $Re_\tau = 932$ and (*b*) for $Re_\tau = 2003$.

fluctuation pairs are aligned or anti-aligned, which is the basis of decomposition (8.1). Whilst it follows immediately from (8.4) that $\Pi_I^v = 0$ if the term inside the x-gradient in that equation is statistically homogeneous, (8.5) shows that $\Pi_I^v = 0$ if $\delta \boldsymbol{u} \cdot \hat{\boldsymbol{r}}$ and $(|\boldsymbol{u}^+|^2 + |\boldsymbol{u}^-|^2)$ are uncorrelated and if $(|\boldsymbol{u}^+|^2 + |\boldsymbol{u}^-|^2)$ is statistically homogeneous. Of course, this is not the only and necessary way for Π_I^v to vanish. In particular, there may be cases of non-homogeneity for which Π_I^v vanishes too, for example, cases where Π_I^v vanishes but Π_I does not.

In figure 14, we plot the terms Π_I^v and Π_H^v in 8.5 normalised by the volume integral of the dissipation. For both Reynolds numbers, we observe that Π_H^v dominates and describes almost perfectly the full interscale transfer Π^v for all scales $r \leq 2y$ in the intermediate range of the channel (y between multiples of δ_ν and approximately half δ). The average interscale transfer from large to small scales is nearly fully described by the negative value of Π_H^v and the inhomogeneity-related interscale transfer rate Π_I^v is close to zero. In a different non-homogenous turbulent flow, the turbulent wake of a square prism, Alves Portela *et al.* (2020) found a significant contribution of the inhomogeneity-related interscale transfer rate to the total interscale transfer rate. It is therefore not trivial that in FD TCF, Π_I^v is negligible compared to Π_H^v in spite of the statistical non-homogeneity of the FD TCF. However, this is partly an artefact of the integration over spheres in $\boldsymbol{r}$-space which we apply to Π_I to obtain Π_I^v. If we lift this integration and use the DNS data to compute $\Pi_I(y, r_1, r_2, r_3)$ as a function of r_2/y for various values of wall-normal distance y and various values of r_1 and r_3, we find (figure 15) that $\Pi_I(y, r_1, r_2, r_3)$ is close to 0 and negligible in most cases except for 'attached eddies', i.e. for values of r_2 relatively close to $2y$ (wall blocking implies $r_2 \leq 2y$) where it is positive, thereby potentially reflecting interscale transfer from small to large scales (similarly to Cimarelli *et al.* 2016; Cho, Hwang & Choi 2018) except for r_2 near-equal to $2y$ where it is negative. The non-vanishing inhomogeneity-related interscale transfer of 'attached eddies' is averaged out when we integrate Π_I to obtain Π_I^v.

Returning to Π_H^v and the fact that it has very similar dependencies on r and y as Π^v, we note, in particular, that Π_H^v has a minimum at the near same $r \approx r_{min}$ where Π^v has a minimum, and even that the minimum value of Π_H^v closely obeys the same relation
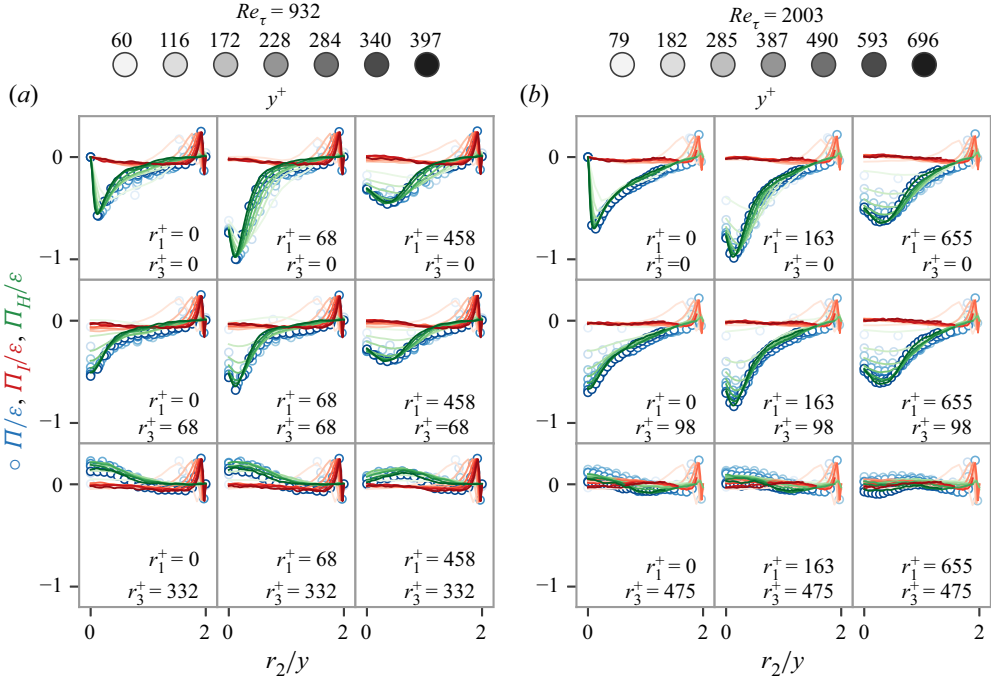
Figure 15. Π (blue markers), Π_I (red lines) and Π_H (green lines) normalised with the two-point dissipation rate ε vs the wall-normal scale r_2 divided with y. (a) $Re_\tau = 932$, from left to right we increase the streamwise scale r_1 and from top to bottom the spanwise scale r_3. (b) Similarly for $Re_\tau = 2003$. Wall-normal distance is increased from light to dark colours.

(6.21) that Π_{min}^v obeys (see figure 16). As seen in § 6, the two-point separation scale $r = r_{min}$ demarcates between smaller values of r where Π^v is balanced by dissipation and viscous diffusion and larger values of r where Π^v is balanced by dissipation and two-point turbulence production. However, the theory of § 6, which is conclusive for Π^v, has no say on Π_H^v and can therefore not explain our observation that Π_H^v behaves very much like Π^v. We therefore adopt a different point of view from that in § 6 and look at PDFs of instantaneous (in time) and local (in (x, z) planes) interscale transfer rates $\pi^v \equiv (3/4\pi) \int (\delta\boldsymbol{u} \cdot \hat{\boldsymbol{r}}/r)|\delta\boldsymbol{u}|^2 \, d\Omega_r$, $\pi_H^v \equiv -(3/2\pi) \int (\delta\boldsymbol{u} \cdot \hat{\boldsymbol{r}}/r)(\boldsymbol{u}^- \cdot \boldsymbol{u}^+) \, d\Omega_r$ and $\pi_I^v \equiv (3/4\pi) \int (\delta\boldsymbol{u} \cdot \hat{\boldsymbol{r}}/r)(|\boldsymbol{u}^+|^2 + |\boldsymbol{u}^-|^2) \, d\Omega_r$. Clearly, $\Pi^v = \langle\pi^v\rangle$, $\Pi_H^v = \langle\pi_H^v\rangle$ and $\Pi_I^v = \langle\pi_I^v\rangle$.

In figure 17, we plot examples of PDFs of π^v, π_H^v and π_I^v for a couple of wall distances y within the intermediate range $\delta_\nu \ll y \ll \delta$ and for different values of separation scale r to see how these PDFs evolve with varying r. As pointed out by Alves Portela *et al.* (2020), at $r = 0$, we have $\Pi^v = \Pi_H^v = \Pi_I^v = 0$. As r progressively increases, the PDFs of π^v and π_H^v move to the left towards increasingly negative values, as shown in the insets of figure 17(*a,b,e,f*). This overall PDF drift is most pronounced at the smaller values of r, and causes Π^v and Π_H^v to progressively decrease below 0 as r increases. However, the skewnesses of the PDFs of π^v and of π_H^v grow from negative values close to -10 at the smallest separations r to values between -1 and even slightly positive as r grows (see figure 18(*a,b,e,f*)). This evolution of the skewnesses of these two PDFs counteracts their overall drift towards increasingly negative values and acts to bring Π^v and Π_H^v back

967 A22-24
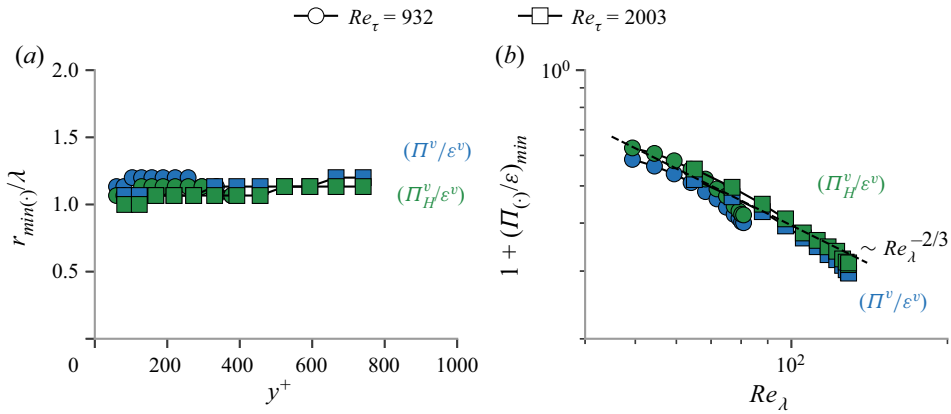
Figure 16. (*a*) Values of r/λ where minima of Π^v/ε^v and minima of Π_H^v/ε^v are observed as functions of wall distance y^+. (*b*) Values of $1 + (\Pi^v/\varepsilon^v)_{min}$ (in blue) and of $1 + (\Pi_H^v/\varepsilon^v)_{min}$ (in green), as functions of Re_λ. Dashed line shows a scaling of $Re_\lambda^{-2/3}$. Circle markers for $Re_\tau = 932$, square markers for $Re_\tau = 2003$.

towards zero as r increases. The minima of Π^v and Π_H^v occur as a result of these two counteracting tendencies, the overall drift dominating at scales r smaller than r_{min} and causing Π^v and Π_H^v to decrease, and the decreasingly skewed PDF dominating at scales larger than r_{min} and causing Π^v and Π_H^v to increase.

The PDF of the inhomogeneity-related interscale transfer rates π_I^v is radically different as far as skewness is concerned (see figure 18). Whilst the PDFs of both π^v and π_H^v are skewed towards forward cascade events at small r and evolve with increasing r towards not being skewed or even being slightly skewed towards inverse cascade events, the PDF of π_I^v is highly skewed towards inverse cascade events at small r and evolves very quickly with increasing r towards not being very skewed. It remains only slightly skewed (positively or negatively) for all permissible r larger than approximately 2λ (the word 'permissible' refers to $r \leq 2y$). The difference is not only that the PDF of π_I^v is oppositely skewed to the PDFs of π^v and π_H^v at small r, but the equally if not even more important difference is that, as r increases, the skewness of π_I^v evolves much faster towards small absolute values (which it actually reaches at $r \approx 2\lambda$) than the skewnesses of π_H^v and π^v which evolve much more gradually towards values around and larger than -1.

However, the PDF of π_I^v is similar to the PDFs of π^v and π_H^v in that they all have an overall drift to the left, i.e. towards forward cascading negative values, as the separation scale r increases (see insets of plots in figure 17). In the case of the inhomogeneity-related interscale energy transfer rate, this overall PDF drift towards forward cascade events is counteracted at small separations r by the significant PDF skewness towards inverse cascade events leading to small values of Π_I^v. As r increases, the drift slows down, and the skewness quickly drops to small absolute values keeping values of Π_I^v small.

In conclusion, the statistics of the inhomogeneity-related interscale transfer rate π_I^v are very different from those of π_H^v and π^v. The PDFs of π_I^v are characterised by a skewness towards inverse cascade events at the small scales in particular, whereas the PDFs of both π_H^v and π^v are characterised by a skewness towards forward cascade events at most scales. These PDFs result in relatively small values of Π_I^v and in very similar dependencies on separation r of Π_H^v and Π^v. As the separation scale r decreases from large values close to $2y$ towards the Taylor length λ, the PDFs of both π_H^v and π^v become increasingly skewed towards forward cascading events and the average values Π_H^v and Π^v become increasingly
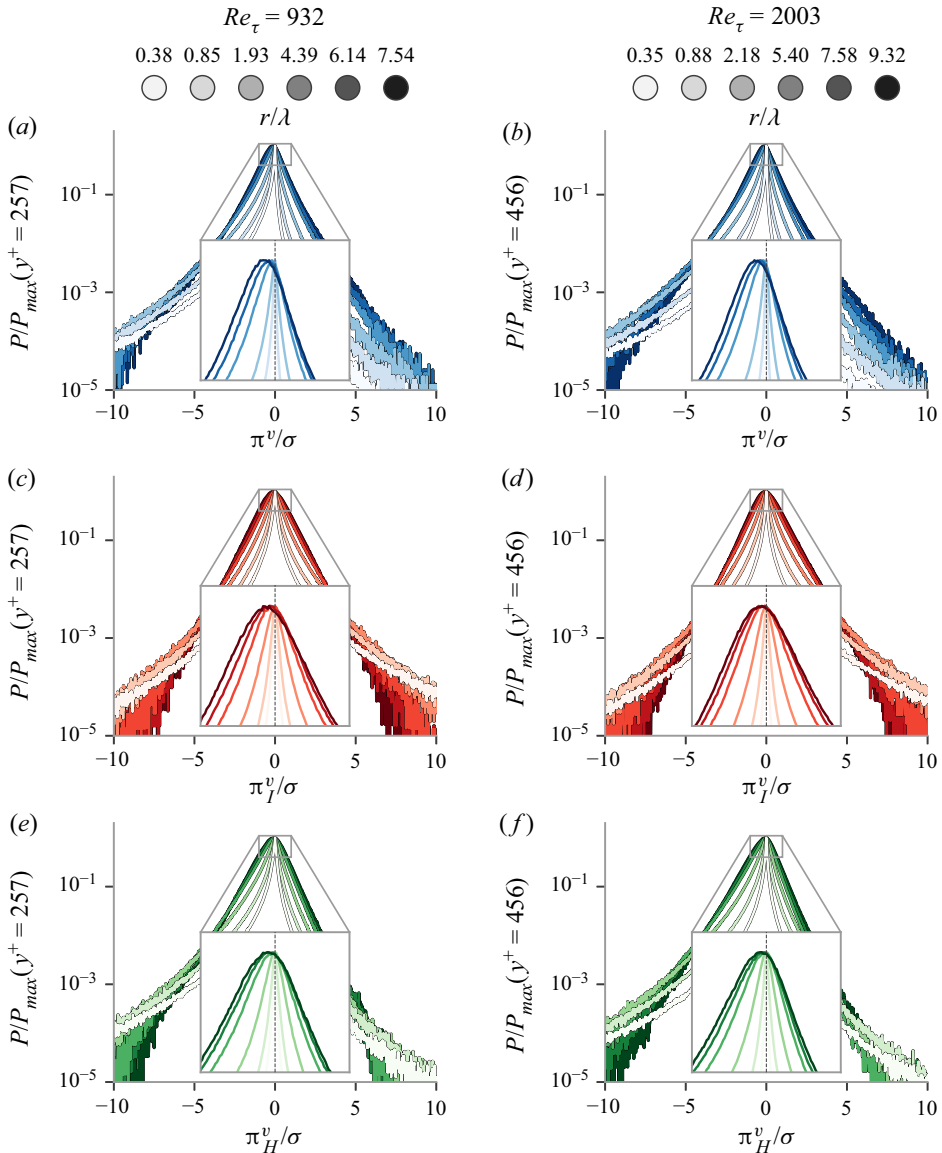
Figure 17. Probability density functions (PDFs) of (*a,b*) π^v, (*c,d*) π_I^v and (*e,f*) π_H^v normalised with their respective maximum probability. The values of the terms are normalised with their own standard deviation. The scale r is increased from light to dark colours. (*a,c,e*) $Re_\tau = 932$, (*b,d,f*) $Re_\tau = 2003$. Inset is a zoom of the area close to the maximum probability in lin–lin axes.

negative. However, as r crosses λ and tends towards even smaller separation lengths below λ, these two PDFs drift towards inverse cascading events in their entirety, thereby bringing the average values of Π_H^v and Π^v back towards zero.

These two counteracting effects of drift and skewness remain and are therefore confirmed if we consider only the tails of the PDFs of π_H^v and π^v. In figure 19(*a,b*), we plot the average values of π_H^v and π^v over the samples of relatively intense values representing only 1 % of all samples. The average of π_H^v over its relatively intense values depends on y and r very much like Π_H^v but with an order of magnitude higher values

967 A22-26
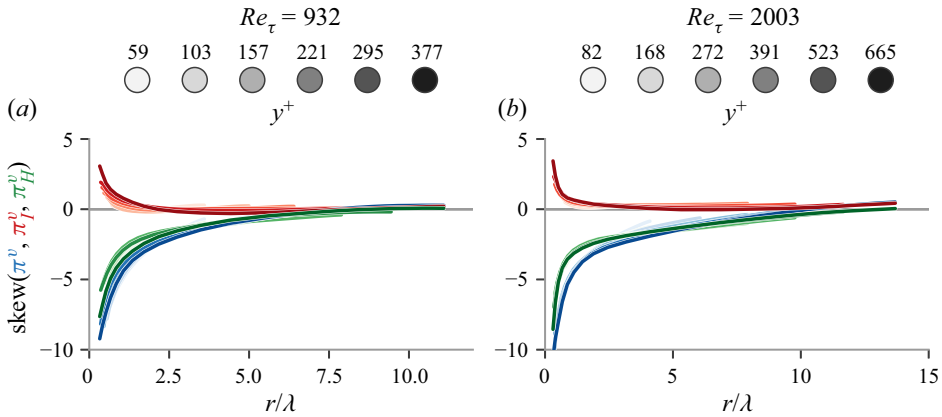
Figure 18. Skewness factor of π^v in blue colours, $\pi_I{}^v$ in red colours and of π_H^v in green colours as a function of r/λ, for different wall-normal locations. The wall-distance y is increased from light to dark colours. (*a*) For $Re_\tau = 932$ and (*b*) for $Re_\tau = 2003$.

(compare with figure 14). However, the average of π_I^v over these relatively intense values is disproportionally affected by the PDF's positive skewness, and is therefore positive or close to zero and higher than Π_I^v in figure 14 as the cancelling effect of the drift is overcome. To concentrate on the drift and minimise the effect of the skewness, in figure 19(*c*,*d*), we report average values of π_H^v, π_I^v and π^v calculated on the basis of only the most probable part of the PDFs representing 20 % of all samples. These average values are an order of magnitude smaller than Π_H^v, Π_I^v and Π^v in figure 14. They are close to zero at the smallest separations r and continuously decrease in negative values till they more or less stabilise at large enough r, reflecting the effect of overall drift of the PDFs towards forward interscale transfers and the fact that this drift stabilises at large enough r. Without the skewness effect, which is not as present around the peaks of the PDFs as in their extreme tails, these conditional averages (figure 19*c*,*d*) do not significantly return towards 0 with increasing r and therefore look very different from Π_H^v, Π_I^v and Π^v in figure 14. The averages Π_H^v, Π_I^v and Π^v in this latter figure emerge as a weighted sum of the conditional averages in figure 19(*a*,*b*) with those in figure 19(*c*,*d*).

Note, finally, that the skewness dominated r-range of the PDFs of π_H^v and π^v coincides with the r-range where Π^v is balanced by turbulent dissipation rate and two-point turbulence production. The root cause of this coincidence may be anti-aligned velocity fluctuation pairs because they enhance two-point turbulence production (§ 5) while also being the seat of a significant skewness towards compressive, i.e. forward cascading, relative motions (§ 8.1). The drift of the PDFs of π_H^v and π^v towards inverse cascades is in fact, a recentering of the PDFs so that their peak values move towards zero and is mostly present in the r-range where Π^v is balanced by turbulent dissipation rate and viscous diffusion (see § 6). At these small scales comparable to λ and below, both aligned and anti-aligned fluctuation pairs contribute significantly to Π^v (see end of § 8.1) and this may be related to the recentring of the PDFs around zero interscale transfer rate.

9. Conclusions

In this paper, we have considered fully developed turbulent channel flow (FD TCF) and have made theoretical predictions concerning its scale-by-scale energy balance averaged
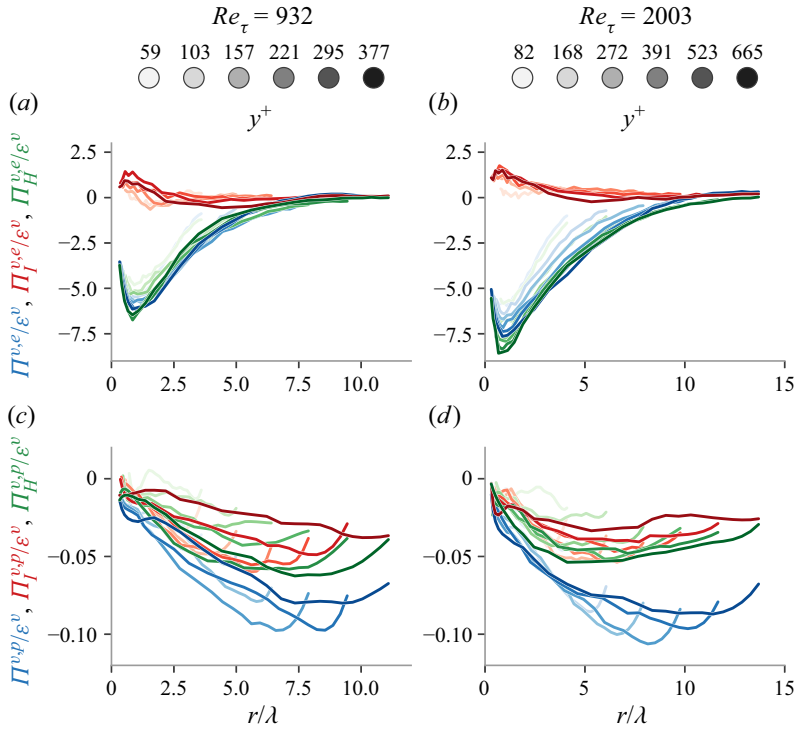
Figure 19. (*a,b*) Averages of most intense events accounting for 1 % of all events for $\Pi^{v,e}$ (blue lines), $\Pi_I^{v,e}$ (red lines) and $\Pi_H^{v,e}$ (green lines). (*c,d*) Averages of most probable events accounting for 20 % of all events for $\Pi^{v,p}$ (blue lines), $\Pi_I^{v,p}$ (red lines) and $\Pi_H^{v,p}$ (green lines). (*a,c*) For $Re_\tau = 932$, (*b,d*) for $Re_\tau = 2003$. Wall-normal distance is increased from light to dark colours.

over spheres in **r**-space in the double limit $Re_\tau \to \infty$, $y^+ \to \infty$ (i.e. $Re_\lambda \sim \lambda/\delta_v \sim (y^+)^{1/2} \to \infty$) with the constraint $y \ll \delta$. At leading order, both the inner and the outer scale-by-scale energy balances involve interscale turbulence energy transfer and turbulence dissipation, but the inner balance is completed with viscous diffusion, whereas the outer balance is completed with two-point turbulence production.

Previous studies already analysed the Kármán–Howarth–Monin–Hill (KHMH) equation for FD TCF. For example, Cimarelli *et al.* (2013, 2016) examined the energy flux path in reduced spaces r_1, r_3 and y with $r_2 = 0$ and r_2, r_3, and y with $r_1 = 0$ (or $r_1 = $ Const. in the case of Gatti *et al.* (2019)). The omission of one scale-space direction prevents this approach from accessing the full interscale transfer picture. Our methodology is different and complementary as it does not omit any scale-space direction but integrates over spheres in full 3-D scale space. Whilst we lose the ability to distinguish between directions in scale space, we gain the capability to access decisive information on interscale energy transfer and forward/inverse cascade which occur normal to the sphere's surface in scale space.

The intermediate layer ($\delta_v \ll y \ll \delta$) of FD TCF is a non-homogeneous but statistically stationary turbulent flow region where interscale turbulence energy transfer has properties similar to interscale turbulence energy transfer in freely decaying (i.e. non-stationary) homogeneous turbulence far from initial conditions. This paper's theory predicts that for any wall-normal distance y in the intermediate layer, Kolmogorov equilibrium is achieved

967 A22-28

asymptotically only around the Taylor length λ (i.e. for scales which are taken to remain a constant multiple of λ in the asymptotic limit) which is not an inertial length given that it depends on viscosity and turbulent kinetic energy at y. A similar conclusion was reached in previous studies of freely decaying homogeneous turbulence far from initial conditions (Lundgren 2002; Obligado & Vassilicos 2019; Meldi & Vassilicos 2021) where, as shown here by (6.19) for the intermediate layer of FD TCF, there are systematic departures from Kolmogorov equilibrium for scales moving away from λ both towards the large eddy size (here y) and towards the local (here in y) Kolmogorov length η. DNS data for FD TDF confirm these conclusions and also confirm the specific scaling predictions (6.20) and (6.21): namely, the interscale transfer rate has a forward cascade peak at $r_{min} \sim \lambda$ where it tends with increasing Reynolds number towards minus turbulence dissipation, i.e. Kolmogorov-type equilibrium, as $Re_\lambda^{-2/3}$. Viscous diffusion is negligible on the large r side of this peak whereas turbulence production is negligible on the small r side of the peak. A similar peak (where production's role is played by the time derivative term defined in § 2) and similar scalings hold in freely decaying homogeneous isotropic turbulence far from initial conditions (Lundgren 2002; Obligado & Vassilicos 2019; Meldi & Vassilicos 2021) but for slightly different though related quantities given that, here, all the terms in the scale-by-scale turbulence energy budget are averaged over spheres of radius r in r-space.

The DNS data show that two-point turbulence production is positive for all $r \le 2y$ and all y in the intermediate layer, and that it increases with two-point separation distance r and decreases with increasing y. The two-point turbulence production is positive mainly because one-point turbulence production is positive even though two-point correlations conditioned on more or less aligned fluctuating velocities act to reduce this positivity. Interestingly, pairs of aligned fluctuating velocities may be expected mostly within sweeps and ejections, which are regions with a major contribution to the positivity of one-point turbulence production (Kline & Robinson 1990; Pope 2000; Wallace 2016). The positivity of two-point turbulence production is in fact enhanced by two-point correlations conditioned on more or less anti-aligned fluctuating velocities, particularly at larger separations r.

The two-point production rate is a functional (see (4.8)) of the second-order anisotropic structure function S_{12} defined by (4.6). This structure function is identically zero in homogeneous isotropic turbulence, but in the intermediate layer of FD TCF, the present theory predicts a leading order $(\varepsilon^v r)^{2/3} \sim u_\tau^2 (r/y)^{2/3}$ behaviour for S_{12} in the range $\eta \ll r \ll y$. The DNS data provide some, though not entirely conclusive, confirmation for this high-Reynolds-number scaling but the values of Re_λ are probably not high enough (between 50 and 120) in the DNS data used here for which Re_τ is approximately 2000 in one case and approximately 1000 in the other.

The present asymptotically high-Reynolds-number theory also leads to a leading order scaling for the second-order structure function S_2 which is similar to the centreline region of some turbulent wakes in terms of the $r^{2/3}$ part of the scaling, but different in terms of the prefactor which is not proportional to the 2/3 power of a turbulence dissipation rate in the centreline region of those turbulent wakes (see Chen & Vassilicos 2022). Different types of non-homogeneity may lead to some important differences in second-order structure function scalings, an issue which merits future attention. The non-homogeneity in the intermediate layer of FD TCF is characterised by significant two-point turbulence production and negligible two-point turbulent transport and pressure-velocity terms, whereas the non-homogeneity on the centreline of turbulent wakes is inverse, i.e. turbulent production is negligible but turbulent transport and pressure-velocity terms are not. Future

attempts at a physically meaningful classification of non-homogeneous turbulent flows may need to start from this paragraph's observations.

The opposing roles played by more or less aligned and more or less anti-aligned pairs of fluctuating velocities in shaping two-point turbulence production have motivated the second part of our DNS study concerning their roles in shaping interscale turbulence energy transfer in the intermediate layer of FD TCF. The interscale turbulence energy is determined by stretching relative motions responsible for inverse transfer from small to large scales and by compressing relative motions responsible for forward transfer from large to small scales. It turns out that more or less aligned fluctuation pairs are stretching relative motions on average, whereas more or less anti-aligned fluctuation pairs are on average compressive relative motions. The relative motions of more or less aligned fluctuation pairs are stretching on average as a result of $\delta \boldsymbol{u}$ having a tendency to be directed in the same direction as the separation vector $\boldsymbol{r}$ for pairs of aligned fluctuating velocities, a tendency which weakens with increasing r irrespective of wall distance y. The relative motions of more or less anti-aligned fluctuation pairs are compressive on average because the fluctuations of $\delta \boldsymbol{u} \cdot \hat{\boldsymbol{r}}$ are skewed towards negative values for such fluctuation pairs. This skewness diminishes with increasing r irrespective of y. Incidentally, more or less aligned fluctuation pairs are much more likely than more or less anti-aligned fluctuation pairs.

Relative motions of more or less aligned fluctuation pairs are maximally stretching on average, and relative motions of more or less anti-aligned fluctuation pairs are maximally compressing on average at a separation length $r = r_m$ which, for all y, is very close to r_{min}, the separation length where Π^v/ε^v has its minimum. Combining the first and second parts of the present study, it appears that in the layer $\delta_\nu \ll y \ll \delta$ of FD TCF, an approach to Kolmogorov-like equilibrium with increasing local Reynolds number may be achieved at those length scales r where aligned fluctuating velocities are stretching with their difference $\delta \boldsymbol{u}$ maximally or near-maximally aligned with the separation vector $\boldsymbol{r}$ and where anti-aligned fluctuations are maximally or near-maximally skewed towards large negative values of $\delta \boldsymbol{u} \cdot \hat{\boldsymbol{r}}$.

Even though more or less aligned fluctuation pairs are on average stretching and are more frequent than more or less anti-aligned fluctuation pairs, they do not dominate interscale turbulence energy transfer, which is nevertheless forward on average, i.e. from large to small scales. This is an effect of small-scale anisotropies. At scales of the order of the Taylor length and larger, the interscale turbulence energy transfer is, in fact, dominated by more or less anti-aligned fluctuations. However, at scales smaller than the Taylor length, the actual value of the interscale turbulence energy transfer rate results from interscale turbulence energy transfers by both aligned (local inverse cascades) and anti-aligned (local forward cascades) fluctuations, both of which are significant and cannot be ignored.

Finally, correlations between stretching/compression relative motions and alignment/anti-alignment of fluctuation pairs determine the spherically averaged (in $\boldsymbol{r}$-space) homogeneous part of the interscale turbulence energy transfer rate introduced by Alves Portela *et al.* (2020). The DNS data of FD TCF used here show that this homogeneous part accounts almost completely for the total spherically averaged interscale turbulence energy transfer rate in the intermediate layer for all separation scales $r \le 2y$, including the scaling with the Taylor length of the separation $r = r_{min}$ where it peaks and the scaling with Re_λ of its peak value, i.e. scalings (6.20) and (6.21). The spherically averaged inhomogeneous part of the interscale turbulence energy transfer is negligible even though the turbulence is significantly non-homogeneous in FD TCF in contrast with the centreline of a turbulent wake which is also non-homogeneous, but differently, and where Alves Portela *et al.* (2020) found a similarly averaged inhomogeneous interscale turbulence energy transfer

967 A22-30

to be significant and, in fact, quite important in the scale-by-scale physics. However, when the spherical average is lifted, the average inhomogeneous interscale transfer rate remains close to zero except for separation components r_2 characterising attached eddies.

By lifting the average over x, z, t, we obtain PDFs of spherically averaged interscale turbulence energy transfer rates and of their homogeneous and inhomogeneous parts. The PDFs of the spherically averaged interscale turbulence energy transfer rates and of their homogeneous part are very similar and vary with r in a very similar way. Their dependence on r is governed by counteracting effects of overall PDF drift towards forward cascade values and of diminishing skewness towards forward cascade events with increasing r. The approach towards Kolmogorov equilibrium occurs at those scales r near the Taylor length where these two counteracting effects balance. The PDFs of spherically averaged inhomogeneous interscale turbulence energy transfer rates are significantly different as they are characterised by a skewness towards inverse rather than forward cascade events at small scales.

As a final comment, one area that may reveal more information on energy transfer in wall-turbulence should be the application of the present paper's framework to individual structural elements of the flow such as intense Reynolds shear stress structures (Lozano-Durán & Jiménez 2014), vortex clusters (del Álamo *et al.* 2006), uniform momentum zones and vortical fissures (Bautista *et al.* 2019).

Author ORCIDs.

- A. Apostolidis https://orcid.org/0000-0002-9078-1490;
- J.P. Laval https://orcid.org/0000-0003-2267-8376;
- J.C. Vassilicos https://orcid.org/0000-0003-1828-6628.

Appendix

We use two methods for the numerical computation of the normalised 3-D integrals of (2.2). The volume integrals that involve divergence in r space are simplified using the Gauss divergence theorem and therefore transformed into surface integrals of the flux across the sphere's surface. We insert a triangulated sphere of 5120 triangles and radius r at each x, y, z point of the DNS grid, corresponding to the centre of the sphere, and interpolate the velocity and its derivatives, using a trilinear interpolation, at the centres of the triangles. Finally, we compute the two-point quantities of interest between the antipodal triangles on our sphere, multiply them with the corresponding surface area of the triangle, sum all the triangles and divide the result with the volume of the discretised sphere.

For the quantities to which we cannot apply the Gauss divergence theorem, we make a local Cartesian grid of $n_{x_l} = 41$, $n_{y_l} = 81$, $n_{z_l} = 41$ points centred at each x, y, z point in space, corresponding to the centre of the sphere, and extending from $-r$ to r in all directions. We then interpolate (with trilinear interpolation) the velocity and its derivatives at every point, which satisfies $\sqrt{x_l^2 + y_l^2 + z_l^2} \leq r$ (x_l, y_l, z_l are the local coordinates), compute the two-point quantities and multiply them with the local volume unit $dV_l = dx_l dy_l dz_l$, sum and divide with the volume of the discretised sphere.

References

DEL ÁLAMO, J.C., JIMÉNEZ, J., ZANDONADE, P. & MOSER, R.D. 2006 Self-similar vortex clusters in the turbulent logarithmic region. *J. Fluid Mech.* **561**, 329.

ALVES PORTELA, F., PAPADAKIS, G. & VASSILICOS, J.C. 2020 The role of coherent structures and inhomogeneity in near-field interscale turbulent energy transfers. *J. Fluid Mech.* **896**, A16.

APOSTOLIDIS, A., LAVAL, J.-P. & VASSILICOS, J.C. 2022 Scalings of turbulence dissipation in space and time for turbulent channel flow. *J. Fluid Mech.* **946**, A41.

BATCHELOR, G.K. 1953 *The Theory of Homogeneous Turbulence*. Cambridge University Press.

BAUTISTA, J.C.C., EBADI, A., WHITE, C.M., CHINI, G.P. & KLEWICKI, J.C. 2019 A uniform momentum zone–vortical fissure model of the turbulent boundary layer. *J. Fluid Mech.* **858**, 609–633.

CHEN, J.G. & VASSILICOS, J.C. 2022 Scalings of scale-by-scale turbulence energy in non-homogeneous turbulence. *J. Fluid Mech.* **938**, A7.

CHO, M., HWANG, Y. & CHOI, H. 2018 Scale interactions and spectral energy transfer in turbulent channel flow. *J. Fluid Mech.* **854**, 474–504.

CIMARELLI, A. & DE ANGELIS, E. 2012 Anisotropic dynamics and sub-grid energy transfer in wall-turbulence. *Phys. Fluids* **24** (1), 015102.

CIMARELLI, A., DE ANGELIS, E. & CASCIOLA, C.M. 2013 Paths of energy in turbulent channel flows. *J. Fluid Mech.* **715**, 436–451.

CIMARELLI, A., DE ANGELIS, E., JIMENEZ, J. & CASCIOLA, C.M. 2016 Cascades and wall-normal fluxes in turbulent channel flows. *J. Fluid Mech.* **796**, 417–436.

COLE, J.D. 1968 *Perturbation Methods in Applied Mathematics*. Blaisdell Publishing Company.

DALLAS, V., VASSILICOS, J.C. & HEWITT, G.F. 2009 Stagnation point von Kármán coefficient. *Phys. Rev. E* **80** (4), 046306.

FRISCH, U. 1995 *Turbulence: The Legacy of A.N. Kolmogorov*. Cambridge University Press.

GATTI, D., REMIGI, A., CHIARINI, A., CIMARELLI, A. & QUADRIO, M. 2019 An efficient numerical method for the generalised Kolmogorov equation. *J. Turbul.* **20** (8), 457–480.

GOTO, S. & VASSILICOS, J.C. 2016 Unsteady turbulence cascades. *Phys. Rev. E* **94** (5), 053108.

HILL, R.J. 2001 Equations relating structure functions of all orders. *J. Fluid Mech.* **434**, 379–388.

HILL, R.J. 2002 Exact second-order structure-function relationships. *J. Fluid Mech.* **468**, 317–326.

HINCH, E.J. 1991 *Perturbation Methods*. Cambridge University Press.

KLINE, S.J. & ROBINSON, S.K. 1990 Quasi-coherent structures in the turbulent boundary layer. I-Status report on a community-wide summary of the data. In *Near-Wall Turbulence*, pp. 200–217. Hemisphere Publishing Corporation, New York.

LEE, M. & MOSER, R.D. 2019 Spectral analysis of the budget equation in turbulent channel flows at high Re. *J. Fluid Mech.* **860**, 886–938.

LESIEUR, M. 1997 *Turbulence in Fluids*. Fluid Mechanics and its Applications, vol. 40. Springer.

LOZANO-DURÁN, A. & JIMÉNEZ, J. 2014 Time-resolved evolution of coherent structures in turbulent channels: characterization of eddies and cascades. *J. Fluid Mech.* **759**, 432–471.

LUNDGREN, T.S. 2002 Kolmogorov two-thirds law by matched asymptotic expansion. *Phys. Fluids* **14** (2), 6.

MARATI, N., CASCIOLA, C.M. & PIVA, R. 2004 Energy cascade and spatial fluxes in wall turbulence. *J. Fluid Mech.* **521**, 191–215.

MELDI, M. & VASSILICOS, J.C. 2021 Analysis of Lundgren's matched asymptotic expansion approach to the Kármán–Howarth equation using the eddy damped quasinormal Markovian turbulence closure. *Phys. Rev. Fluids* **6** (6), 064602.

OBLIGADO, M. & VASSILICOS, J.C. 2019 The non-equilibrium part of the inertial range in decaying homogeneous turbulence. *Europhys. Lett.* **127** (6), 64004.

POPE, S.B. 2000 *Turbulent Flows*. Cambridge University Press.

SAGAUT, P. & CAMBON, C. 2018 *Homogeneous Turbulence Dynamics*. Springer.

SREENIVASAN, K.R. 1984 On the scaling of the turbulence energy dissipation rate. *Phys. Fluids* **27** (5), 1048–1051.

STEIROS, K. 2022 Balanced nonstationary turbulence. *Phys. Rev. E* **105** (3), 035109.

TAYLOR, G.I. 1935 Statistical theory of turbulence. *Proc. R. Soc. Lond.* A **151** (873), 421–444.

TOWNSEND, A.A. 1976 *The Structure of Turbulent Shear Flow*, 2nd edn. Cambridge University Press.

VAN DYKE, M.D. 1964 *Perturbation Methods in Fluid Mechanics*. Academic Press.

VASSILICOS, J.C. 2015 Dissipation in turbulent flows. *Annu. Rev. Fluid Mech.* **47** (1), 95–114.

VASSILICOS, J.C., LAVAL, J.-P., FOUCAUT, J.-M. & STANISLAS, M. 2015 The streamwise turbulence intensity in the intermediate layer of turbulent pipe flow. *J. Fluid Mech.* **774**, 324–341.

WALLACE, J.M. 2016 Quadrant analysis in turbulence research: history and evolution. *Annu. Rev. Fluid Mech.* **48** (1), 131–158.

YUVARAJ, R. 2022 Analysis of energy cascade in wall-bounded turbulent flows. PhD thesis, Centrale Lille Institut.

ZHOU, Y. & VASSILICOS, J.C. 2020 Energy cascade at the turbulent/nonturbulent interface. *Phys. Rev. Fluids* **5**, 064604.

ZIMMERMAN, S.J., ANTONIA, R.A., DJENIDI, L., PHILIP, J. & KLEWICKI, J.C. 2022 Approach to the 4/3 law for turbulent pipe and channel flows examined through a reformulated scale-by-scale energy budget. *J. Fluid Mech.* **931**, A28.